Study of $\eta' \to \pi^+\pi^- l^+l^-$ decays at BESIII

The BESIII collaboration

E-mail: besiii-publications@ihep.ac.cn

ABSTRACT: With a sample of $(10087 \pm 44) \times 10^6$ J/ψ events accumulated with the BESIII detector, we analyze the decays $\eta' \to \pi^+\pi^- l^+l^-(l = e, \mu)$ via the process $J/\psi \to \gamma\eta'$. The branching fractions are measured to be $\mathcal{B}(\eta' \to \pi^+\pi^- e^+e^-) = (2.45 \pm 0.02(\text{stat.}) \pm 0.08(\text{syst.})) \times 10^{-3}$ and $\mathcal{B}(\eta' \to \pi^+\pi^- \mu^+\mu^-) = (2.16 \pm 0.12(\text{stat.}) \pm 0.06(\text{syst.})) \times 10^{-5}$, and the ratio is $\frac{\mathcal{B}(\eta' \to \pi^+\pi^- e^+e^-)}{\mathcal{B}(\eta' \to \pi^+\pi^- \mu^+\mu^-)} = 113.4 \pm 0.9(\text{stat.}) \pm 3.7(\text{syst.})$. In addition, by combining the $\eta' \to \pi^+\pi^- e^+e^-$ and $\eta' \to \pi^+\pi^- \mu^+\mu^-$ decays, the slope parameter of the electromagnetic transition form factor is measured to be $b_{\eta'} = 1.30 \pm 0.19$ $(\text{GeV}/c^2)^{-2}$, which is consistent with previous measurements from BESIII and theoretical predictions from the VMD model. The asymmetry in the angle between the $\pi^+\pi^-$ and l^+l^- decay planes, which has the potential to reveal the CP-violation originating from an unconventional electric dipole transition, is also investigated. The asymmetry parameters are determined to be $\mathcal{A}_{CP}(\eta' \to \pi^+\pi^- e^+e^-) = (-0.21 \pm 0.73(\text{stat.}) \pm 0.01(\text{syst.}))\%$ and $\mathcal{A}_{CP}(\eta' \to \pi^+\pi^- \mu^+\mu^-) = (0.62 \pm 4.71(\text{stat.}) \pm 0.08(\text{syst.}))\%$, implying that no evidence of CP-violation is observed at the present statistics. Finally, an axion-like particle is searched for via the decay $\eta' \to \pi^+\pi^- a, a \to e^+e^-$, and upper limits of the branching fractions are presented for the mass assumptions of the axion-like particle in the range of $0 - 500$ MeV/c^2.

Contents

1 Introduction

The $\eta' \to \pi^+\pi^- l^+l^-$ (with $l = e$ or μ) decays are of great interest in both theoretical and experimental research as they involve contributions from the box-anomaly of quantum chromodynamics (QCD), and can be used to probe the transition form factors (TFFs) [1]. The TFF is a momentum transfer (q^2) dependent function, which describes the complex internal structure or the full set of intermediate processes that contribute to a reaction. At low-momentum transfer, the TFF is particularly important to determine the low-energy parameters of these mesons, such as the slope parameter $b_{\eta'}$ [2], which plays a critical role in determining the electromagnetic interaction radius. The vector meson dominance (VMD) model leads to the expectation $b_{\eta'} \approx \frac{1}{m_V^2}$ for the $P \to \gamma\gamma^\star$ decay [2, 3], where m_V is a light vector meson mass. Also, the TFF is of utmost importance because it determines the size of hadronic quantum corrections in the calculation of the anomalous magnetic moment of the muon, $(g-2)_\mu$ [2]. Theoretically, the $\eta' \to \pi^+\pi^- l^+l^-$ decays have been investigated with different models, including the hidden gauge model [1], the chiral unitary approach [4] and the VMD models [1]. Experimentally, CLEO and BESIII have measured the branching fractions of these decays using 4.0×10^4 and 6.8×10^6 η' events, respectively. Different

	$\mathcal{B}(\eta' \to \pi^+\pi^- e^+e^-)$ (10^{-3})	$\mathcal{B}(\eta' \to \pi^+\pi^- \mu^+\mu^-)$ (10^{-5})
Hidden gauge [1]	2.17 ± 0.21	2.20 ± 0.30
VMD [1]	2.27 ± 0.13	2.41 ± 0.25
Unitary χPT [2]	$2.13^{+0.17}_{-0.31}$	$1.57^{+0.96}_{-0.75}$
CLEO [5]	$2.50^{+1.2}_{-0.9} \pm 0.5$	< 24
BESIII (2013) [6]	$2.11 \pm 0.12 \pm 0.15$	< 2.9
BESIII (2021) [7, 8]	$2.42 \pm 0.05 \pm 0.08$	$1.97 \pm 0.33 \pm 0.19$

Table 1. Different theoretical predictions and previous experimental results of $\mathcal{B}(\eta' \to \pi^+\pi^- l^+l^-)$.

theoretical predictions and previous experimental results of the branching fractions ($\mathcal{B}$) are listed in table 1.

In 2000, the KTeV Collaboration observed a large CP-violation in the distribution of the T-odd angle φ in $K_L^0 \to \pi^+\pi^- e^+e^-$ decay [9], where φ is the angle between the e^+e^- decay plane and the $\pi^+\pi^-$ decay plane in the K_L^0 center-of-mass system. The interference between the CP-conserving and CP-violating amplitudes generates an angular distribution proportional to $\sin 2\varphi$ [1]. Similarly, this asymmetry can be measured from the decays of other pseudoscalar mesons, such as the η'. It was first explored in the decay $\eta' \to \pi^+\pi^- e^+e^-$ in the BESIII experiment, and the CP-violating asymmetry ($\mathcal{A}_{CP}$) was determined to be $(2.9 \pm 3.7 \pm 1.1)\%$ [8], which is consistent with zero.

Additionally, the hadronic decay channels of η' mesons could include a signal of a QCD axion, dark photon or other hadronically coupled Axion-like particle (ALP). Among the most promising modes are the three-body final states $\pi^+\pi^- a$, which have been studied recently [10, 11]. The ATOMKI experiment reported an anomaly in the angular correlation spectra in ^{8}Be [12] and ^{4}He [13] nuclear transitions. A light pseudoscalar particle a decaying to e^+e^- [14–16] was proposed to explain the anomaly. An ALP could also cause a deviation from the expected value of the electron anomalous magnetic moment [17–19].

With ten billion J/ψ data events collected with the BESIII detector during 2009-2019 [20], we can improve the precision of the branching fraction measurements, measure the TFFs and search for CP-violation and hadronically coupled ALPs.

2 BESIII detector

The BESIII detector [21] records symmetric e^+e^- collisions provided by the BEPCII storage ring [22] in the center-of-mass energy range from 2.0 to 4.95 GeV, with a peak luminosity of 1×10^{33} cm^{-2}s^{-1} achieved at $\sqrt{s} = 3.77$ GeV. BESIII has collected large data samples in this energy region [23]. The cylindrical core of the BESIII detector covers 93% of the full solid angle and consists of a helium-based multilayer drift chamber (MDC), a plastic scintillator time-of-flight system (TOF), and a CsI(Tl) electromagnetic calorimeter (EMC), which are all enclosed in a superconducting solenoidal magnet providing a 1.0 T magnetic field. The magnetic field was 0.9 T in 2012, which affects 11% of the total J/ψ data. The solenoid is supported by an octagonal flux-return yoke with resistive plate counter muon

Decay mode	Generator model
$J/\psi \to \gamma\eta'$	Helicity amplitude
$\eta' \to \pi^+\pi^- l^+ l^-$	VMD model [35]
$\eta' \to \pi^+\pi^-\pi^+\pi^-$	ChPT and VMD model [36]
$\eta^{(\prime)} \to \gamma\pi^+\pi^-$	Amplitude analyses [37]
$\eta' \to \eta\pi^+\pi^-$	Dalitz plot analyses [38]
$\eta \to \gamma\mu^+\mu^-$	Electromagnetic form factor [39]

Table 2. Generator models used for MC simulations.

identification modules interleaved with steel. The charged-particle momentum resolution at 1 GeV/c is 0.5%, and the dE/dx resolution is 6% for electrons from Bhabha scattering. The EMC measures photon energies with a resolution of 2.5% (5%) at 1 GeV in the barrel (end cap) region. The time resolution in the TOF barrel region is 68 ps, while that in the end cap region was 110 ps. The end cap TOF system was upgraded in 2015 using multigap resistive plate chamber technology, providing a time resolution of 60 ps [24], which benefits 87% of the data used in this analysis.

3 Data sample and Monte Carlo simulation

This analysis is based on $(10087 \pm 44) \times 10^6$ J/ψ events collected with the BESIII detector [20], which yields a sample of about 5.3×10^7 η' events though the radiative decay $J/\psi \to \gamma\eta'$.

The estimation of background contributions and the determination of detection efficiencies are performed with Monte Carlo (MC) simulations. The BESIII detector is modeled with GEANT4 [25–27]. The production of the J/ψ resonance is implemented with MC event generator KKMC [28, 29], while the decays are simulated by EVTGEN [30, 31]. The possible backgrounds are studied using a sample of J/ψ inclusive events in which the known decays of J/ψ are modeled with branching fractions being set to the world average values given by the Particle Data Group (PDG) [32], while unknown decays are generated with the LUNDCHARM model [33, 34]. Specific generators have been developed in this analysis, and the corresponding theoretical models are listed in table 2. The signal samples of sizes 1×10^6 and 5×10^5 are used for $\eta' \to \pi^+\pi^- e^+ e^-$ and $\eta' \to \pi^+\pi^- \mu^+\mu^-$ decays, separately.

4 Event selection and background analysis

The final state of interest is studied through the decay chain $J/\psi \to \gamma\eta', \eta' \to \pi^+\pi^- l^+ l^-$. Each event is required to contain at least one good photon candidate, and four charged track candidates with a total charge of zero. Charged tracks detected in the MDC are required to be within a polar angle (θ) range of $|\cos\theta| \leq 0.93$, where θ is defined with respect to the z-axis, which is the symmetry axis of the MDC. Each charged track is required to have the point of closest approach to the interaction point (IP) within ± 1 cm in the plane perpendicular to beam direction and within ± 10 cm in z direction.
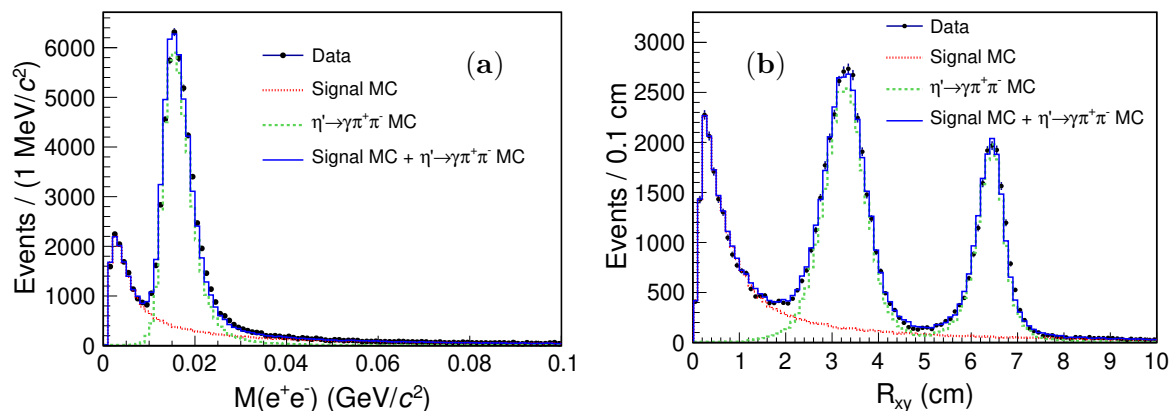
Figure 1. The distributions of (a) the e^+e^- invariant mass spectrum and (b) the distance of the e^+e^-−vertex from the IP in the transverse direction after applying the χ^2_{4C+PID} condition. The dots with error bars represent the data, the red dotted histograms are the MC signal shapes, the green dashed histograms are the $J/\psi \to \gamma\eta', \eta' \to \gamma\pi^+\pi^-$ MC shapes, and the blue solid histograms are the sums of the MC signal and MC background from $J/\psi \to \gamma\eta', \eta' \to \gamma\pi^+\pi^-$. Both of these MC simulations are normalized to the yields found in table 3.

Photons are reconstructed from showers in the EMC exceeding a deposited energy of 25 MeV in the barrel region ($|\cos\theta| < 0.8$) and 50 MeV in the endcap regions ($0.86 < |\cos\theta| < 0.92$). The angle between the shower position and any charged tracks extrapolated to the EMC must be greater than 15 degrees. Finally, photons are required to arrive within 700 ns from the event start time in order to reduce background from photons that do not originate from the same event.

For each signal candidate, particle identification (PID) is performed using the TOF and dE/dx information, and four-constraint (4C) kinematic fits are performed imposing energy and momentum conservation under the hypotheses of $\gamma\pi^+\pi^-e^+e^-$ and $\gamma\pi^+\pi^-\mu^+\mu^-$ final states. The variable, $\chi^2_{4C+PID} = \chi^2_{4C} + \sum_{i=1}^{4} \chi^2_{PID(i)}$, is used to select the best candidate if the event contains more than one. Here χ^2_{4C} and χ^2_{PID} represent the Chi-square of the 4C kinematic fit and PID, respectively, and i corresponds to the charged track candidates in each hypothesis (pion, electron, or muon). For each event, the candidate with the smallest $\chi^2_{4C+PID}(\pi^+\pi^-l^+l^-)$ is kept for further analysis.

For the $\eta' \to \pi^+\pi^-e^+e^-$ decay, $\chi^2_{4C+PID}(\gamma\pi^+\pi^-e^+e^-) < 60$ is required, which has been optimized with respect to the figure of merit $N_S/\sqrt{N_D}$, where N_S is the number of events in the signal MC sample, and N_D is the number of events in data. The primary peaking background comes from $J/\psi \to \gamma\eta', \eta' \to \gamma\pi^+\pi^-$ events, where a photon converts to an e^+e^- pair at the beam pipe or the inner wall of the MDC. One might expect the invariant mass of such a conversion pair, $M(e^+e^-)$, to be close to zero for this kind of background. However, the BESIII tracking algorithm uses the IP as a reference point for all tracks, which means that the direction of tracks that originate elsewhere are mis-reconstructed. Hence, a conversion pair gains an artificial opening angle, and the reconstructed invariant mass is larger than the true value. Therefore, the conversion background appears as a large peak at about $0.015 \, \text{GeV}/c^2$ in the $M(e^+e^-)$ distribution, shown in figure 1 (a).
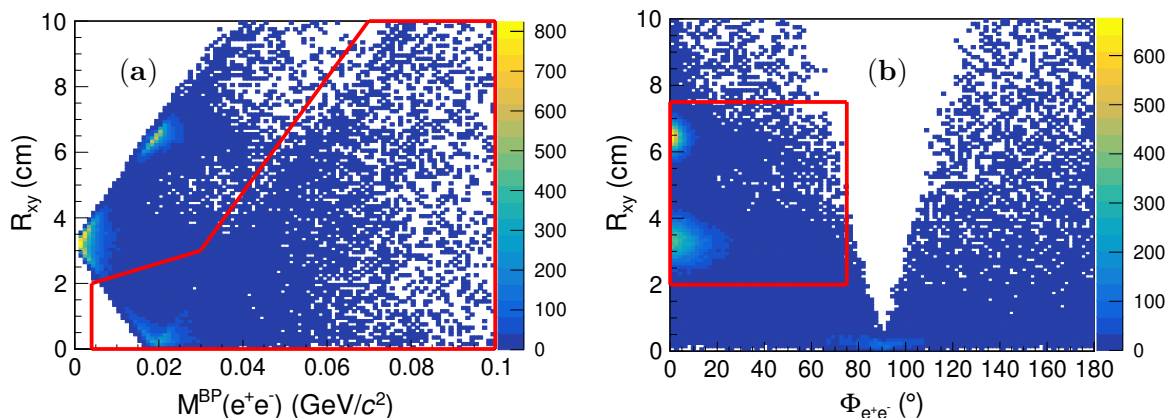
Figure 2. Photon conversion veto criterion on the (a) R_{xy} vs. $M^{\mathrm{BP}}(e^+e^-)$ and (b) R_{xy} vs. Φ_{ee} plots from data. All events above (left plot) or inside (right plot) the red solid polygons are rejected.

The intersection of the e^+- and e^--helices in the $r-\phi$ projection provides the distance from the e^+e^--vertex position to the IP, R_{xy} [40]. Figure 1 (b) shows the R_{xy} distribution for the selected events, where e^+e^- pairs peak at three characteristic locations in the detector. The signal pairs originate from the IP, whereas the conversion background pairs are at $R_{xy} \approx 3$ cm, corresponding to the beam pipe, and at $R_{xy} \approx 6$ cm, corresponding to the inner wall of the MDC.

In order to reject photon conversion events and improve the signal-to-background ratio, two additional variables are introduced. The first one is the invariant mass of the e^+e^- pair at the beam pipe, $M^{\mathrm{BP}}(e^+e^-)$, which is determined by changing the reference point of the helices of all $e^\pm$ tracks to their respective points of intersection with the beam pipe, and subsequently recalculating the momentum vectors. This changes the direction of the vectors, but not their magnitudes. The momenta of the e^+e^- pair that is created at the beam pipe will instead be approximately parallel and the invariant mass close to the mass of two electrons. The second variable is the opening angle of the e^+e^- pair in the $x-y$ plane, Φ_{ee} [41]. For the e^+e^- pairs that originate from the IP, such as $\eta' \to \pi^+\pi^- e^+e^-$ decays, the opening angles determined with the calculated momentum vectors are increased, and as a consequence, their invariant masses become larger than the true value. For conversion events, Φ_{ee} is expected to be close to zero. In the two-dimensional distributions of R_{xy} vs. $M^{\mathrm{BP}}(e^+e^-)$, and R_{xy} vs. Φ_{ee}, shown in figure 2, signal events and photon conversion events are well separated. By selecting appropriate regions of these distributions, the photon conversion events are vetoed. First, we select all events to the high mass side of a curve defined by straight line segments between the points $(0.004\,\mathrm{GeV}/c^2, 0\,\mathrm{cm})$, $(0.004\,\mathrm{GeV}/c^2, 2\,\mathrm{cm})$, $(0.03\,\mathrm{GeV}/c^2, 3$ cm), and $(0.07\,\mathrm{GeV}/c^2, 10\,\mathrm{cm})$ in the R_{xy} vs. $M^{\mathrm{BP}}(e^+e^-)$ distribution. Then, we reject the events from $\Phi_{ee} < 75°$ when 2 cm $< R_{xy} < 7.5$ cm. The effects of the photon conversion veto, have been estimated in MC simulations, and it removes 98.6% of the $\eta' \to \pi^+\pi^-\gamma$ conversion background, while retaining $\sim 86\%$ of the $\eta' \to \pi^+\pi^- e^+e^-$ signal.

For the $\eta' \to \pi^+\pi^-\mu^+\mu^-$ decay, $\chi^2_{4\mathrm{C}}(\gamma\pi^+\pi^-\mu^+\mu^-) < 25$ is required, and $\chi^2_{4\mathrm{C+PID}}(\gamma\pi^+\pi^-\mu^+\mu^-)$ is required to be less than $\chi^2_{4\mathrm{C+PID}}(\gamma\pi^+\pi^-\pi^+\pi^-)$ to suppress background from $J/\psi \to \gamma\pi^+\pi^-\pi^+\pi^-$. The comparison of the $\mu^+\mu^-$ mass spectrum between data
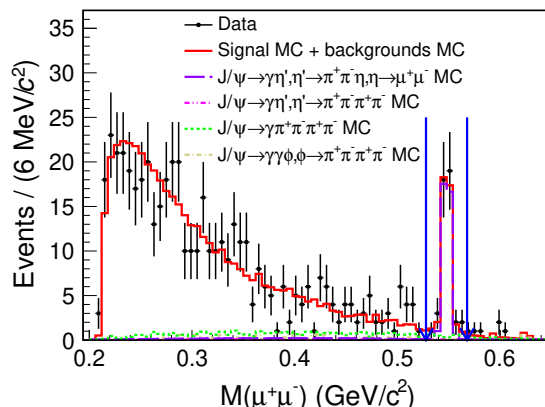
Figure 3. The $\mu^+\mu^-$ invariant mass distribution for events satisfying 0.945 GeV/c^2 < $M(\pi^+\pi^-\mu^+\mu^-)$ < 0.975 GeV/c^2. The dots with error bars represent the data, the purple dashed histogram is the $J/\psi \to \gamma\eta', \eta' \to \pi^+\pi^-\eta, \eta \to \mu^+\mu^-$ MC shape, the pink dotted histogram is the $J/\psi \to \gamma\eta', \eta' \to \pi^+\pi^-\pi^+\pi^-$ MC shape, the green dashed histogram is the $J/\psi \to \gamma\pi^+\pi^-\pi^+\pi^-$ MC shape, the golden dotted histogram is the $J/\psi \to \gamma\gamma\phi, \phi \to \pi^+\pi^-\pi^+\pi^-$ MC shape, and the red solid histogram is the sum of the MC signals and all MC backgrounds.

and MC simulation in figure 3, where 0.945 GeV/c^2 < $M(\pi^+\pi^-\mu^+\mu^-)$ < 0.975 GeV/c^2 has been required, shows good agreement. To suppress the background from $\eta' \to \pi^+\pi^-\eta, \eta \to \mu^+\mu^-$, we require $|M(\mu^+\mu^-) - 0.548| > 0.02$ GeV/c^2.

Possible background events are analyzed with the same procedure using the inclusive MC sample, and they mainly originate from the background processes listed in table 3. For the dominant background channels, dedicated exclusive MC samples are generated to estimate their contributions to the $\pi^+\pi^- l^+ l^-$ invariant mass spectrum in figure 4. For the $\mathcal{B}$ determination, we require the fit range of 0.91 GeV/c^2 < $M(\pi^+\pi^- e^+ e^-)$ < 1.0 GeV/c^2 and 0.9 GeV/c^2 < $M(\pi^+\pi^-\mu^+\mu^-)$ < 1.0 GeV/c^2 for the $\eta' \to \pi^+\pi^- e^+ e^-$ and $\eta' \to \pi^+\pi^-\mu^+\mu^-$ decays, respectively. In the measurements of the TFF, $\mathcal{A}_{CP}$ and search for ALPs, we further require 0.945 GeV/c^2 < $M(\pi^+\pi^- e^+ e^-)$ < 0.97 GeV/c^2 and 0.945 GeV/c^2 < $M(\pi^+\pi^-\mu^+\mu^-)$ < 0.975 GeV/c^2 for the $\eta' \to \pi^+\pi^- e^+ e^-$ and $\eta' \to \pi^+\pi^-\mu^+\mu^-$ decays, respectively. The aim is to minimize background interference and preserve the signals as much as possible.

5 Branching fraction measurements

To determine the numbers of the $\eta' \to \pi^+\pi^- l^+ l^-$ events, an unbinned maximum likelihood fits are performed to the $\pi^+\pi^- l^+ l^-$ invariant mass spectra. The branching fractions of $\eta' \to \pi^+\pi^- l^+ l^-$ are determined by

$$\mathcal{B}(\eta' \to \pi^+\pi^- l^+ l^-) = \frac{N_{\text{sig}}}{N_{J/\psi} \times \mathcal{B}(J/\psi \to \gamma\eta') \times \varepsilon}, \quad (5.1)$$

where N_{sig} are the signal yields determined from data, ε are the detection efficiencies for the decays $\eta' \to \pi^+\pi^- l^+ l^-$, which are determined from the simulated samples, $\mathcal{B}(J/\psi \to \gamma\eta')$ is the branching fraction of $J/\psi \to \gamma\eta'$, $(5.21 \pm 0.17) \times 10^{-3}$ [32] and $N_{J/\psi}$ is the number of J/ψ events, $(10087 \pm 44) \times 10^6$ [20].

Signal channels	Main background channels	Sample sizes	Normalized events	
			$\mathcal{B}$	TFF/$\mathcal{A}_{CP}$/ALPs
$\eta' \to \pi^+\pi^- e^+ e^-$	$J/\psi \to \gamma\eta', \eta' \to \gamma\pi^+\pi^-$	2.3×10^7	672 ± 22	598 ± 20
$\eta' \to \pi^+\pi^- \mu^+\mu^-$	$J/\psi \to \gamma\eta', \eta' \to \pi^+\pi^-\eta, \eta \to \mu^+\mu^-$	5×10^5	11 ± 1	9 ± 1
	$J/\psi \to \gamma\eta', \eta' \to \pi^+\pi^-\pi^+\pi^-$	2.3×10^5	206 ± 2	3 ± 1
	$J/\psi \to \gamma\eta', \eta' \to \pi^+\pi^-\eta, \eta \to \gamma\pi^+\pi^-$	5×10^6	24 ± 2	—
	$J/\psi \to \gamma\pi^+\pi^-\pi^+\pi^-$	4.8×10^5	—	36 ± 11
	$J/\psi \to \gamma\gamma\phi, \phi \to \pi^+\pi^-\pi^+\pi^-$	4.8×10^6	—	10 ± 2

Table 3. Main background processes and their corresponding normalized events of the $\eta' \to \pi^+\pi^- l^+ l^-$ decays. For the $\mathcal{B}$ determination, "—" indicates that the number of background events are left floating in the fit. In the measurements of the TFF, $\mathcal{A}_{CP}$ and search for ALPs, "—" indicates that the background channel is disregarded due to the extremely low number of background events in the signal mass range.

For the $\eta' \to \pi^+\pi^- e^+ e^-$ decay fit, the signal is represented by the MC shape convolved with a Gaussian function to account for the difference in resolution between data and MC simulation. The peaking background arising from the photon conversion process $\eta' \to \gamma\pi^+\pi^-$ is described by the MC simulation shape, and the number of background events, which are listed in table 3, are fixed according to the branching fractions from the PDG [32]. Combinatorial background is represented by a first-order Chebychev polynomial. The fit result shown in figure 4 (a) yields 22725 ± 155 signal events. The goodness of fit is studied using a χ^2 test and the χ^2 value per number of degrees of freedom (ndf) is found to be $\chi^2/ndf = 95.4/95.0$. With a detection efficiency of $(17.49 \pm 0.04)\%$, the branching fraction of $\eta' \to \pi^+\pi^- e^+ e^-$ is calculated to be $(2.45 \pm 0.02) \times 10^{-3}$, where the uncertainties are statistical only.

For the $\eta' \to \pi^+\pi^- \mu^+\mu^-$ decay fit, the shapes of signal and $J/\psi \to \gamma\pi^+\pi^-\pi^+\pi^-$ are taken from the MC simulation. From a topological analysis, possible backgrounds arise from the $J/\psi \to \gamma\gamma\phi, \phi \to \pi^+\pi^-\pi^+\pi^-$ decay in the η' mass distribution around $1\,\text{GeV}/c^2$. A MC sample of $J/\psi \to \gamma\gamma\phi, \phi \to \pi^+\pi^-\pi^+\pi^-$ is generated to describe these backgrounds. The magnitude of the $J/\psi \to \gamma\gamma\phi, \phi \to \pi^+\pi^-\pi^+\pi^-$ and $J/\psi \to \gamma\pi^+\pi^-\pi^+\pi^-$ backgrounds are determined from the fit. All other background events, which are listed in table 3, are fixed according to the branching fractions from the PDG [32]. The fit result shown in figure 4 (b) yields 434 ± 25 signal events, and the goodness of fit is found to be $\chi^2/ndf = 88.9/97.0$. With a detection efficiency of $(37.95 \pm 0.07)\%$, the branching fraction of $\eta' \to \pi^+\pi^- \mu^+\mu^-$ is calculated to be $(2.16 \pm 0.12) \times 10^{-5}$, where the uncertainties are statistical only.

6 Transition form factor measurements

6.1 VMD model

The $\eta' \to \pi^+\pi^- l^+ l^-$ decays are similar to $\eta' \to \gamma\pi^+\pi^-$, in which the photon is replaced by an off-shell one that decays into a $l^+ l^-$ pair. Within the VMD model, it is factorized into three separate parts [1], as illustrated in figure 5. The contact term represents the contribution
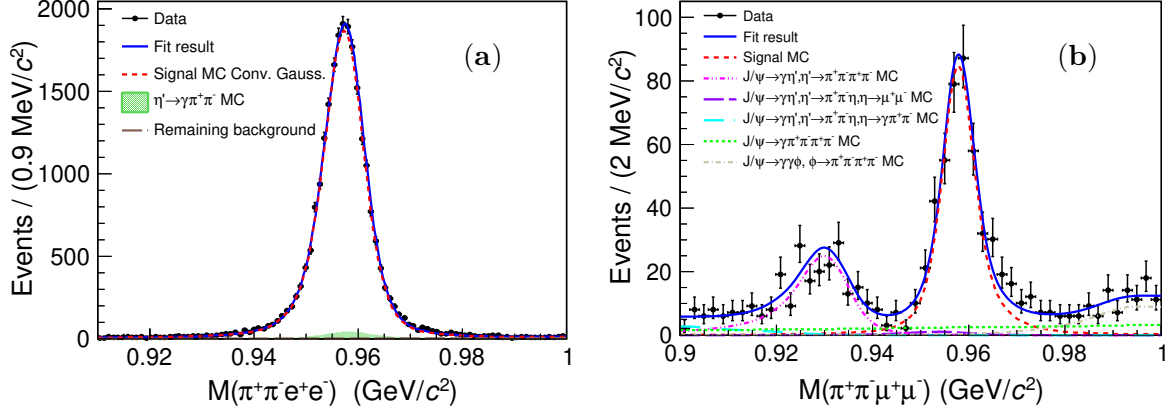
Figure 4. Fits to the invariant mass distributions of (a) $\pi^+\pi^-e^+e^-$ and (b) $\pi^+\pi^-\mu^+\mu^-$. The dots with error bars represent the data, and the blue solid lines are the total fit result. For the $\eta' \to \pi^+\pi^-e^+e^-$ decay, the red dashed histogram represents the MC signal shape convolved with a Gaussian function, the green area is the $J/\psi \to \gamma\eta', \eta' \to \gamma\pi^+\pi^-$ MC shape, and the brown dashed histogram represents the remaining background described by the first-order Chebychev polynomial. For the $\eta' \to \pi^+\pi^-\mu^+\mu^-$ decay, the red dashed histogram represents the MC signal shape, the pink dotted histogram is the $J/\psi \to \gamma\eta', \eta' \to \pi^+\pi^-\pi^+\pi^-$ MC shape, the purple dashed histogram is the $J/\psi \to \gamma\eta', \eta' \to \pi^+\pi^-\eta, \eta \to \mu^+\mu^-$ MC shape. The light blue dotted histogram is the $J/\psi \to \gamma\eta', \eta' \to \pi^+\pi^-\eta, \eta \to \gamma\pi^+\pi^-$ MC shape, the green dashed histogram is the $J/\psi \to \gamma\pi^+\pi^-\pi^+\pi^-$ MC shape, and the golden dotted histogram is the $J/\psi \to \gamma\gamma\phi, \phi \to \pi^+\pi^-\pi^+\pi^-$ MC shape.
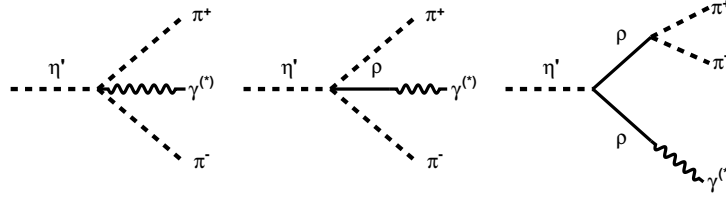

Figure 5. Contact term corresponding to the axial anomaly (left) and other VMD contributions (middle and right) to the decay $\eta' \to \pi^+\pi^-\gamma^*$ [1].

from the axial anomaly, and the other two diagrams give the VMD interactions where the pseudoscalar does not interact directly with the photon.

The four-momenta for the decays $\eta'(P) \to \pi^+(p_+)\pi^-(p_-)l^+(k_+)l^-(k_-)$ are defined as $P = p_+ + p_- + k_+ + k_-$ [42]. The relevant variables are written as

$$s_{\pi\pi} = (p_+ + p_-)^2, \qquad\qquad s_{ll} = (k_+ + k_-)^2. \tag{6.1}$$

$$\beta_\pi = \sqrt{1 - \frac{4M^2(\pi^+\pi^-)}{s_{\pi\pi}}}, \qquad\qquad \beta_l = \sqrt{1 - \frac{4M^2(l^+l^-)}{s_{ll}}}. \tag{6.2}$$

The squared decay amplitude is given as [35]

$$\overline{|\mathcal{A}_{\eta'\to\pi^+\pi^-l^+l^-}|}^2(s_{\pi\pi}, s_{ll}, \theta_\pi, \theta_l, \varphi) = \frac{e^2}{8k^2}|\mathcal{M}(s_{\pi\pi}, s_{ll})|^2 \times \lambda(M^2(\eta'), s_{\pi\pi}, s_{ll}) \\ \times [1 - \beta_l^2 \sin^2\theta_l \sin^2\varphi]s_{\pi\pi}\beta_\pi^2\sin^2\theta_\pi, \tag{6.3}$$

to the leading order with only the magnetic term. The high order corrections with the electric term and the mixing term are visibly smaller than the leading one [1]. Here θ_π is the polar angle of the p_+ in the p_+p_- rest frame with respect to the flight direction of the p_+p_- in the P rest frame, θ_l is the polar angle of the k_- in the k_+k_- rest frame with respect to the flight direction of the k_+k_- in the P rest frame, and φ is the azimuthal angle between the plane formed by p_+p_- in the P rest frame and the corresponding plane formed by the k_+k_- [43, 44]. The Källén function λ is defined as $\lambda(a, b, c) = a^2 + b^2 + c^2 - 2(ab + bc + ca)$. The magnetic form factor $\mathcal{M}(s_{\pi\pi}, s_{ll})$ is given by

$$\mathcal{M}(s_{\pi\pi}, s_{ll}) = \mathcal{M}_{\text{mix}} \times \text{VMD}(s_{\pi\pi}, s_{ll}), \tag{6.4}$$

where $\mathcal{M}_{\text{mix}}$ is the pseudoscalar mesons mixing parameter [1], $\text{VMD}(s_{\pi\pi}, s_{ll})$ is the VMD factor [1, 45] and derived from the VMD model with finite-width corrections as [46]

$$\begin{aligned} \text{VMD}(s_{\pi\pi}, s_{ll}) = 1 &- \frac{3}{4}(c_1 - c_2 + c_3) + \frac{3}{4}(c_1 - c_2 - c_3) \times \frac{m_V^2}{m_V^2 - s_{ll} - im_V\Gamma(s_{ll})} \\ &+ \frac{3}{2}c_3 \frac{m_{V,\pi}^2}{m_{V,\pi}^2 - s_{\pi\pi} - im_{V,\pi}\Gamma(s_{\pi\pi})} \times \frac{m_V^2}{m_V^2 - s_{ll} - im_V\Gamma(s_{ll})}. \end{aligned} \tag{6.5}$$

Here m_V and $m_{V,\pi}$ are the masses of the vector meson $V(V \to l^+l^-)$ and $V_\pi(V_\pi \to \pi^+\pi^-)$, respectively. The parameters c_{1-3} are model dependent and determine the contributions of the different interaction terms illustrated in figure 5. Γ is its total width [35] as

$$\Gamma(s) = g\left(\frac{\sqrt{s}}{m_{V,i}}\right)\left(\frac{1 - \frac{4m_i^2}{s}}{1 - \frac{4m_i^2}{m_{V,i}^2}}\right)^{\frac{3}{2}} \Theta(s - 4m_i^2) \ (i = l \text{ or } \pi; \ V, i = V \text{ or } V, \pi), \tag{6.6}$$

where $g = 149.1 \, \text{MeV}$, and Θ is the Heaviside step function.

6.2 Analysis method and background treatment

Unbinned maximum likelihood fits to the e^+e^- and $\pi^+\pi^-$ mass spectra are performed to determine the fit parameters in the VMD factor given in eq. (6.5). The probability-density function (PDF) to observe the i-th event characterized by the measured four-momenta ξ_i of the particles in the final state is

$$\mathcal{P}(\xi_i) = \frac{|\mathcal{A}(\xi_i)|^2\varepsilon(\xi_i)}{\int |\mathcal{A}(\xi)|^2\varepsilon(\xi)\mathrm{d}\xi}, \tag{6.7}$$

where $\mathcal{A}$ is the amplitude as shown in eq. (6.3), and $\varepsilon(\xi_i)$ is the detection efficiency. The fit minimizes the negative log-likelihood value

$$-\ln\mathcal{L} = -\omega'[\sum_{i=1}^{N_{\text{data}}} \ln\mathcal{P}(\xi_i) - \omega_{\text{bkg1}}\sum_{j=1}^{N_{\text{bkg1}}} \ln\mathcal{P}(\xi_j) - \omega_{\text{bkg2}}\sum_{k=1}^{N_{\text{bkg2}}} \ln\mathcal{P}(\xi_k) - \ldots], \tag{6.8}$$

where i run over all accepted data, and j, k, ... run over the other considered background events. There corresponding number of events are denoted by N_{data}, N_{bkg1} and N_{bkg2}.

$\omega_{\text{bkg1}} = \frac{N'_{\text{bkg1}}}{N_{\text{bkg1}}}$ and $\omega_{\text{bkg2}} = \frac{N'_{\text{bkg2}}}{N_{\text{bkg2}}}$ are the weights of the backgrounds, where N'_{bkg1} and N'_{bkg2} are their contributions according to branching fractions taken from PDG. To obtain an unbiased uncertainty estimation, the normalization factor ω' [47] is considered, described as

$$\omega' = \frac{N_{\text{data}} - N_{\text{bkg1}}\omega_{\text{bkg1}} - N_{\text{bkg2}}\omega_{\text{bkg2}}}{N_{\text{data}} + N_{\text{bkg1}}\omega_{\text{bkg1}}^2 + N_{\text{bkg2}}\omega_{\text{bkg2}}^2}. \tag{6.9}$$

For the $\eta' \to \pi^+\pi^- e^+ e^-$ decay, the number of the background events of $J/\psi \to \gamma\eta', \eta' \to \gamma\pi^+\pi^-$ is fixed according to the branching fractions from the PDG [32], and the non-peaking background distribution is estimated by using the η' one-dimensional sideband events. The sideband is defined as $M(\pi^+\pi^- e^+ e^-) \in [0.915, 0.9275] \bigcup [0.985, 0.9975]$ GeV/c^2. For the $\eta' \to \pi^+\pi^- \mu^+\mu^-$ decay, the number of the background events of $J/\psi \to \gamma\pi^+\pi^-\pi^+\pi^-$ is obtained by fitting the mass spectrum of $\pi^+\pi^-\mu^+\mu^-$, and other backgrounds yields are fixed according to the branching fractions from the PDG [32]. All the numbers of the background events, which are listed in table 3, are obtained in the η' mass regions, 0.945 GeV/$c^2 < M(\pi^+\pi^- e^+ e^-) < 0.97$ GeV/c^2 and 0.945 GeV/$c^2 < M(\pi^+\pi^-\mu^+\mu^-) < 0.975$ GeV/c^2.

6.3 Fit results

By adjusting the values of the c_i-parameters [48], we can switch between various VMD models:

- Hidden gauge model (Model I): $c_1 - c_2 = c_3 = 1$;

- Full VMD model (Model II): $c_1 - c_2 = 1/3, c_3 = 1$;

- Modified VMD model (Model III): $c_1 - c_2 \neq c_3$.

Since the dominant contribution is from ρ^0 and its width is large, the parameterization of its shape plays a vital role in describing the $e^+ e^-$ and $\pi^+\pi^-$ mass spectra. For $\eta' \to \pi^+\pi^- e^+ e^-$, the ρ^0 contribution is insufficient to describe the $\pi^+\pi^-$ mass spectra of data and an extra contributions from ω is necessary. If the $\omega \to \pi^+\pi^-$ decay is taken into account, the propagator is written as

$$\frac{m_{V,\pi}^2}{m_{V,\pi}^2 - s_{\pi\pi} - im_{V,\pi}\Gamma(s_{\pi\pi})} + \beta e^{i\theta}\frac{m_\omega^2}{m_\omega^2 - s_{\pi\pi} - im_\omega\Gamma_\omega}, \tag{6.10}$$

where $\beta e^{i\theta}$ is the complex coupling parameter, and $\Gamma_\omega = 8.68$ MeV, which is taken from the PDG [32].

The fit results of the three models mentioned above are summarized in table 4 and table 5, while those of Model I are shown in figure 6 and figure 7. Based on Model I, we calculate a weighted average of $b_{\eta'} = 1.30 \pm 0.19$ (GeV/c^2)$^{-2}$ for $\eta' \to \pi^+\pi^- e^+ e^-$ and $\eta' \to \pi^+\pi^-\mu^+\mu^-$ combined, where the uncertainty is obtained by combining statistical and systematic uncertainties. A test is also made with c_1, c_2, c_3 floating but with $c_1 - c_2 = c_3$ [48]. The fit to our data gives $c_1 - c_2 = c_3 = 1.03 \pm 0.03$, which is consistent with the assumption of the hidden gauge model. Due to the limited statistics in the high $e^+ e^-$ mass region, the statistical uncertainties of m_V for the three models and $c_1 - c_2$ for Model III are relatively large. At present, the fit results can not distinguish between the models.
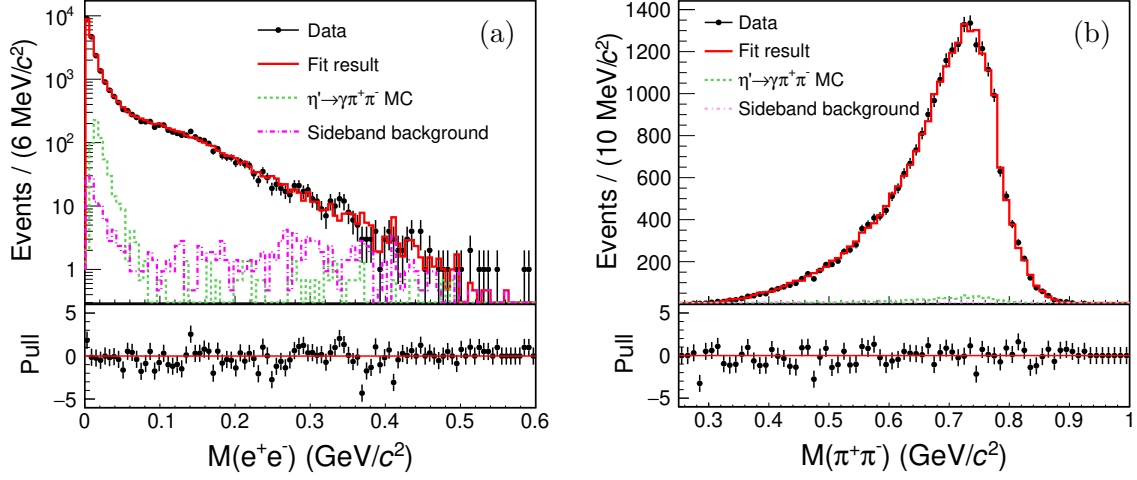
Figure 6. Fits to the invariant mass distributions of (a) e^+e^- and (b) $\pi^+\pi^-$ for $\eta' \to \pi^+\pi^-e^+e^-$ with $c_1 - c_2 = c_3 = 1$ (Model I). The dots with error bars represent data, and the red solid histogram are the total fit results. The green dashed histogram are the $J/\psi \to \gamma\eta', \eta' \to \gamma\pi^+\pi^-$ MC shapes, and the pink dotted histogram are the backgrounds obtained from the η' sideband.
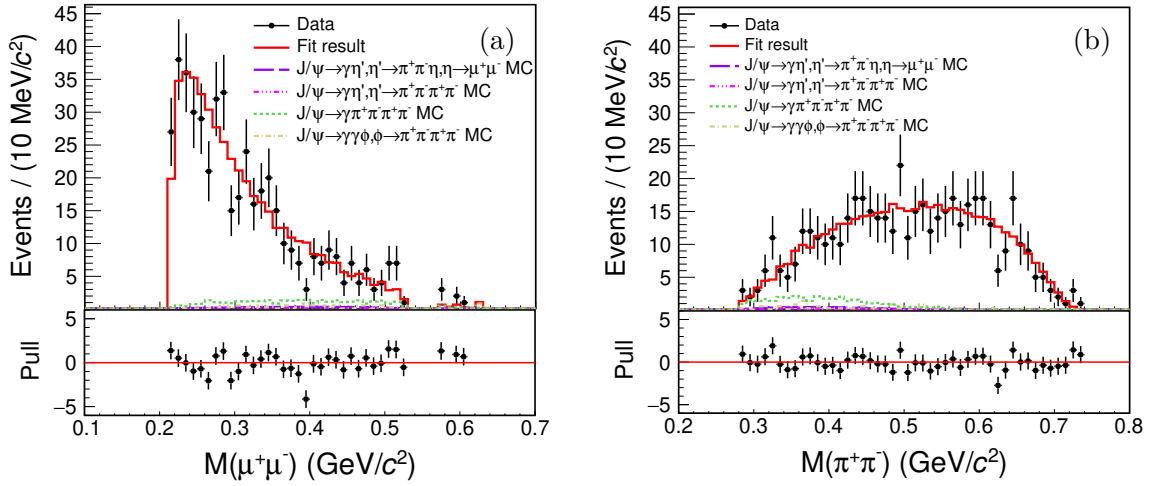

Figure 7. Fits to the invariant mass distributions of (a) $\mu^+\mu^-$ and (b) $\pi^+\pi^-$ for $\eta' \to \pi^+\pi^-\mu^+\mu^-$ with $c_1 - c_2 = c_3 = 1$ (Model I). The dots with error bars represent data, and the red solid histogram are the total fit result. The purple dashed histogram are the $J/\psi \to \gamma\eta', \eta' \to \pi^+\pi^-\eta, \eta \to \mu^+\mu^-$ MC shapes, the pink dotted histogram are the $J/\psi \to \gamma\eta', \eta' \to \pi^+\pi^-\pi^+\pi^-$ MC shapes, the green dashed histogram are the $J/\psi \to \gamma\pi^+\pi^-\pi^+\pi^-$ MC shapes, and the golden dotted histogram are the sums of the other background MC shapes.

$\eta' \to \pi^+\pi^- e^+ e^-$	Model I	Model II	Model III
	$c_1 - c_2 = c_3 = 1$	$c_1 - c_2 = 1/3, c_3 = 1$	$c_1 - c_2 \neq c_3$
$m_V(\mathrm{MeV}/c^2)$	$954.3 \pm 87.8 \pm 36.4$	857.4 ± 76.5	787.5 ± 173.9
$m_{V,\pi}(\mathrm{MeV}/c^2)$	$765.3 \pm 1.2 \pm 20.2$	765.4 ± 1.2	764.8 ± 1.3
$m_\omega(\mathrm{MeV}/c^2)$	$778.7 \pm 1.3 \pm 17.3$	778.7 ± 1.3	778.7 ± 1.4
$\beta(10^{-3})$	$8.5 \pm 1.4 \pm 0.7$	8.5 ± 1.4	8.1 ± 1.5
θ	$1.4 \pm 0.3 \pm 0.1$	1.4 ± 0.3	1.4 ± 0.3
$c_1 - c_2$	1	$1/3$	-0.03 ± 1.09
c_3	1	1	1.03 ± 0.03
$\chi^2/ndof(e^+e^-, \pi^+\pi^-)$	$77.9/82.0,\ 47.8/65.0$	$78.7/82.0,\ 47.6/65.0$	$79.4/82.0,\ 45.1/65.0$
$b_{\eta'}(\mathrm{GeV}/c^2)^{-2}$	$1.10 \pm 0.20 \pm 0.07$	1.36 ± 0.24	1.61 ± 0.71

Table 4. The TFF fit results of the $\eta' \to \pi^+\pi^- e^+ e^-$ decay.

$\eta' \to \pi^+\pi^- \mu^+ \mu^-$	Model I	Model II	Model III
	$c_1 - c_2 = c_3 = 1$	$c_1 - c_2 = 1/3, c_3 = 1$	$c_1 - c_2 \neq c_3$
$m_V(\mathrm{MeV}/c^2)$	$649.4 \pm 55.9 \pm 35.6$	601.6 ± 25.7	589.6 ± 25.9
$m_{V,\pi}(\mathrm{MeV}/c^2)$	$757.3 \pm 24.1 \pm 18.0$	765.4 ± 18.8	774.4 ± 43.5
$c_1 - c_2$	1	$1/3$	0.01 ± 0.45
c_3	1	1	0.98 ± 0.40
$\chi^2/ndof(\mu^+\mu^-, \pi^+\pi^-)$	$48.1/34.0,\ 32.9/46.0$	$48.3/34.0,\ 32.9/46.0$	$49.7/35.0,\ 32.4/46.0$
$b_{\eta'}(\mathrm{GeV}/c^2)^{-2}$	$2.37 \pm 0.41 \pm 0.27$	2.76 ± 0.24	2.88 ± 0.25

Table 5. The TFF fit results of the $\eta' \to \pi^+\pi^- \mu^+ \mu^-$ decay.

7 CP-violating asymmetry

The mixed term between the CP-violating electric and CP-preserving magnetic form factors in the squared amplitude has a φ dependence [8, 9]. According to the squared invariant decay amplitude [1], a fitting function is constructed as

$$F(\varphi) = 1 + b \cdot \sin^2 \varphi + c \cdot \sin 2\varphi, \tag{7.1}$$

where $1 + b \cdot \sin^2 \varphi$ is a dominant contribution from the magnetic term, and $c \cdot \sin 2\varphi$ is from the mixing term, which is the CP-violating term. The asymmetry parameter $\mathcal{A}_{CP}$ is defined as

$$
\begin{aligned}
\mathcal{A}_{CP} &= \frac{1}{\Gamma} \int_0^{2\pi} \frac{d\Gamma}{d\varphi} \mathrm{sign}(\sin 2\varphi) d\varphi \\
&= \frac{\int_{-\pi}^{\pi} F(\varphi) \mathrm{sign}(\sin 2\varphi) d\varphi}{\int_{-\pi}^{\pi} F(\varphi) d\varphi} \\
&= \frac{4c}{(2+b)\pi},
\end{aligned}
\tag{7.2}
$$

Decay channels	b	c	$\mathcal{A}_{CP}(\%)$	$\chi^2/ndof$
$\eta' \to \pi^+\pi^- e^+e^-$	-0.72 ± 0.01	-0.002 ± 0.007	-0.21 ± 0.73	$82.8/96.0$
$\eta' \to \pi^+\pi^- \mu^+\mu^-$	-0.35 ± 0.10	0.008 ± 0.061	0.62 ± 4.71	$71.3/97.0$

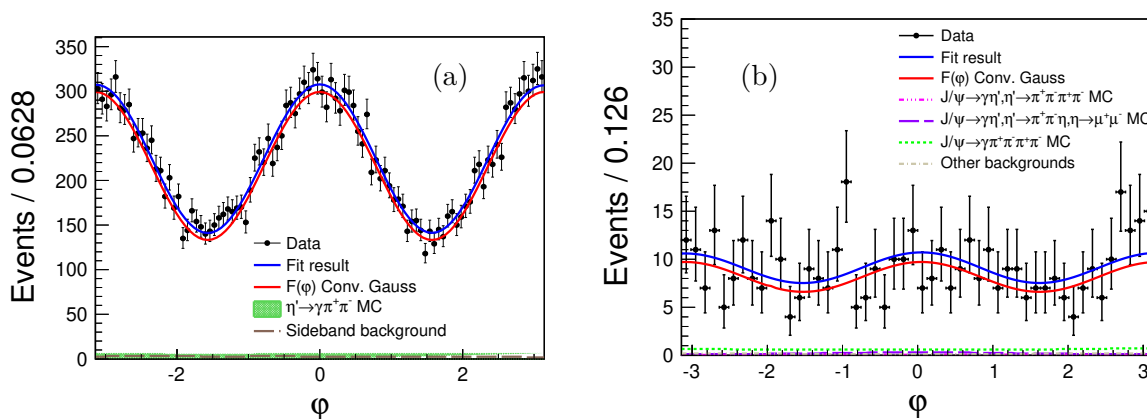**Table 6.** The final results of $\mathcal{A}_{CP}$ for the $\eta' \to \pi^+\pi^- e^+e^-$ decay.

Figure 8. Fits to the φ angle distributions for the (a) $\eta' \to \pi^+\pi^- e^+e^-$ and (b) $\eta' \to \pi^+\pi^- \mu^+\mu^-$ decays. The dots with error bars represent data, the blue solid line are the total fit results, and the red dashed histograms represents the function shapes of $F(\varphi)$ convolved with a Gaussian function. For $\eta' \to \pi^+\pi^- e^+e^-$, the green area is the $J/\psi \to \gamma\eta', \eta' \to \gamma\pi^+\pi^-$ MC shape, and the brown dotted histogram is the background obtained from η' sideband. For $\eta' \to \pi^+\pi^- \mu^+\mu^-$, the pink dotted histogram is the $J/\psi \to \gamma\eta', \eta' \to \pi^+\pi^-\pi^+\pi^-$ MC shape, the purple dashed histogram is the $J/\psi \to \gamma\eta', \eta' \to \pi^+\pi^-\eta, \eta \to \mu^+\mu^-$ MC shape, the green dashed histogram is the $J/\psi \to \gamma\pi^+\pi^-\pi^+\pi^-$ MC shape, and the golden dotted histogram is the sum of the other background MC shapes.

where $\text{sign}(x)$ is a sign function. The parameters b and c and the asymmetry parameter $\mathcal{A}_{CP}$ are obtained by fitting the φ angle distribution, as shown in figure 8. In the fit, the efficiency corrected $F(\varphi)$ function is convolved with a Gaussian function, $f(x; 0, \sigma) = \frac{1}{\sigma\sqrt{2\pi}}\exp(-\frac{x^2}{2\sigma^2})$, to account for the φ resolution, where σ are determined to be 0.035 and 0.030 for $\eta' \to \pi^+\pi^- e^+e^-$ and $\eta' \to \pi^+\pi^- \mu^+\mu^-$, respectively, according to MC simulation.

The background treatment is the same as that in the TFF measurement in section 6.2, and the normalized background events are listed in table 3. The final results are listed in table 6, where the uncertainties are statistical only. These imply that no CP-violation evidence is found at the present level of statistics.

8 Systematic uncertainties of $\mathcal{B}$, $\mathcal{A}_{CP}$ and TFF

We consider possible sources of systematic uncertainties for the measurement of $\mathcal{B}$, $\mathcal{A}_{CP}$ and TFF. The corresponding contributions are discussed in detail below and listed in table 7.

- Number of J/ψ events: the number of J/ψ events is determined to be $(10087 \pm 44) \times 10^6$ from the inclusive hadron events, and the uncertainty of this number is 0.4% [20].

- Branching fraction of $J/\psi \to \gamma\eta'$: the uncertainty from the branching fraction of $J/\psi \to \gamma\eta'$ from the PDG [32] is 1.3%.

- MDC tracking: the data-MC efficiency difference for pion track-finding has been studied using a control sample of $J/\psi \to \pi^+\pi^-\pi^0$. Since the muon mass is similar to that of the pion, we take the same efficiency difference as the pion for the tracking of the muon. For the electron tracking, a mixed sample of $e^+e^- \to e^+e^-\gamma$ at the J/ψ meson mass and $J/\psi \to e^+e^-\gamma_{\mathrm{FSR}}$ processes is used. The data-MC difference, $\Delta_{\mathrm{syst.}}$, is determined as a function of the particle momentum and the cosine of the polar angle. We calculated the uncertainty of $\Delta_{\mathrm{syst.}}$ using the uncertainty propagation formula, and the result is 1.8% as the systematic uncertainty for the $\mathcal{B}$ measurement. Subsequently, each event in the MC samples is re-weighted by a factor $(1 + \Delta_{\mathrm{syst.}})$. The $\mathcal{A}_{\mathrm{CP}}$ are recalculated with efficiencies determined from the re-weighted MC sample. For the TFF measurement, a re-weighted MC sample is used to calculate the MC integral, and a group of new fit results are obtained by using the fit method as in section 6.2. The differences with the nominal results are taken as the systematic uncertainties.

- PID: the difference in the PID efficiencies for the $\eta' \to \pi^+\pi^-\mu^+\mu^-$ decay between data and MC simulation is evaluated in the same way as for the MDC tracking efficiency above. The control sample of $J/\psi \to \pi^+\pi^-\pi^0$ is used to study the pion PID. For the muon PID, we take the same difference as that of the pion.

- Photon detection efficiency: the systematic uncertainty from the reconstruction of photons has been studied extensively in the process $e^+e^- \to \gamma\mu^+\mu^-$. The systematic uncertainty due to photon reconstruction efficiency, defined as the relative difference in efficiencies between data and MC simulation, is observed to be up to the level of 0.5% in both the barrel and end-cap regions.

- Kinematic fit: to investigate the systematic uncertainty associated with the 4C kinematic fit, the track helix parameter correction method [49] is used for $\eta' \to \pi^+\pi^-\mu^+\mu^-$. Half of the difference in the detection efficiencies with and without the helix correction is taken as the systematic uncertainty.

- Combined PID and kinematic fit: the control sample of $J/\psi \to \pi^+\pi^-\pi^0, \pi^0 \to \gamma e^+e^-$ is used to study the systematic uncertainty due to the requirement of $\chi^2_{\mathrm{4C+PID}} < 60$ for $\eta' \to \pi^+\pi^- e^+e^-$. The difference of efficiencies with and without the $\chi^2_{\mathrm{4C+PID}}$ selection between data and MC simulation, 2.0%, is taken as the systematic uncertainty.

- Photon conversion veto: the systematic uncertainty from photon conversion veto has been studied with a clean control sample of $J/\psi \to \pi^+\pi^-\pi^0, \pi^0 \to \gamma e^+e^-$. The relative difference of efficiencies associated with the photon conversion rejection between data and MC simulation, 1.0%, is taken as the systematic uncertainty [50].

- Generator model: the signal MC sample was generated with $c_1 - c_2 = c_3 = 1$. To estimate the systematic uncertainty from generator model, we used the fit results of the modified VMD model in section 6.3 to produce the MC sample, and the difference of

detection efficiency between the modified model ($c_1 - c_2 \neq c_3$) and the nominal models ($c_1 - c_2 = c_3 = 1$) is taken as the uncertainty.

- η' signal range: to estimate the uncertainties from the η' mass range, we perform alternative fits changing the lower and upper boundaries of the η' mass range independently by 0.02 GeV/c^2 for $\eta' \to \pi^+\pi^- e^+ e^-$, 0.01 GeV/$c^2$ for $\eta' \to \pi^+\pi^- \mu^+\mu^-$. The resultant largest differences to the nominal results are taken as the systematic uncertainties.

- Background model: in the fit, the events for some backgrounds are fixed according to the branching fractions from the PDG [32]. To estimate the effect of the uncertainties of the used branching fractions, a set of random numbers have been generated within the uncertainty of each branching fraction. Using these random scaling parameters, a series of fits to the invariant mass distributions of $\pi^+\pi^- e^+ e^-$ or $\pi^+\pi^- \mu^+\mu^-$ mass are performed. The largest changes of the signal yields are taken as the systematic uncertainties.

- Signal shape: in the $\mathcal{B}$ measurement, we use the double or three Gaussian functions instead of the signal MC shapes to fit the $\pi^+\pi^- l^+ l^-$ mass spectrum. The differences in the $\mathcal{B}$ values are taken as the systematic uncertainties.

- Resolution: in the $\mathcal{A}_{\rm CP}$ measurement, to estimate the uncertainty from the resolution, we perform alternative fits changing the resolution from -1.0σ to 1.0σ with an interval of 0.25σ for the $\eta' \to \pi^+\pi^- e^+ e^-$ and $\eta' \to \pi^+\pi^- \mu^+\mu^-$ decays. The largest differences from the nominal results are taken as the systematic uncertainties of the asymmetry parameters.

- Width of ρ and ω: in the TFF measurement, the widths of ρ and ω are taken as constants. The differences of the fit results between fixed and free widths are taken as the systematic uncertainties.

9 Upper limit for ALPs in decay of $\eta' \to \pi^+\pi^- a, a \to e^+ e^-$

To study possible ALPs decaying into $e^+ e^-$, we perform 50 simulations of the signal process $a \to e^+ e^-$ with varied masses of a in steps of 10 MeV/c^2 from 0 to 500 MeV/c^2. Using the hypothesis of a pseudoscalar ALP, the signal process $\eta' \to \pi^+\pi^- a$ and $a \to e^+ e^-$ is generated with the events distributed evenly in the phase space. The MC shapes are determined from the sum of all background contributions plus the 50 groups of different signal MC shapes with a masses from $0 - 500$ MeV/c^2. The η' signal region is defined as 0.945 GeV/$c^2 < M(\pi^+\pi^- e^+ e^-) < 0.97$ GeV/c^2.

We consider possible sources for multiplicative systematic uncertainties of the upper limit for ALPs, such as number of J/ψ events (0.4%), branching fraction of $J/\psi \to \gamma\eta'$ (1.3%), MC statistics (0.1%), MDC tracking (1.3%-7.5%), photon detection efficiency (0.5%), combined PID and kinematic fit (2.0%) and photon conversion veto (1.0%). The total multiplicative systematic uncertainties are $3.0\% - 7.9\%$. The additive systematic uncertainties are considered by alternative fit ranges and background models. The maximum number of signal events among the different fit scenarios is adopted to calculate the upper limit of the signal yield.

Source	$\eta' \to \pi^+\pi^- e^+e^-$ (%)			$\eta' \to \pi^+\pi^- \mu^+\mu^-$ (%)		
	$\mathcal{B}$	$\mathcal{A}_{CP}$	m_V	$\mathcal{B}$	$\mathcal{A}_{CP}$	m_V
Number of J/ψ events	0.4	—	—	0.4	—	—
$\mathcal{B}(J/\psi \to \gamma\eta')$	1.3	—	—	1.3	—	—
MDC tracking	1.8	—	0.2	0.7	—	2.0
PID	—	—	—	1.3	—	2.0
Photon detection	0.5	—	—	0.5	—	—
4C kinematic fit	—	3.7	—	0.6	0.0	1.1
Combined PID and kinematic fit	2.0	—	2.0	—	—	—
Photon conversion veto	1.0	—	1.0	—	—	—
Generator model	0.1	—	—	0.1	—	—
η' mass range	0.4	—	—	1.4	—	—
Background model	0.1	0.1	1.5	0.5	0.2	3.5
Signal shape	1.0	—	—	1.4	—	—
Resolution	—	4.0	—	—	12.7	—
Widths of ρ and ω	—	—	2.7	—	—	3.0
Total	3.4	5.4	3.8	3.0	12.7	5.5

Table 7. The systematic uncertainties in the measurements of $\mathcal{B}$, $\mathcal{A}_{CP}$ and m_V.

Since no evident a signal seen in the $M(e^+e^-)$ distribution, we compute upper limits on the branching ratio, $R^{\text{UP}} = \frac{\mathcal{B}(\eta' \to \pi^+\pi^- a) \cdot \mathcal{B}(a \to e^+e^-)}{\mathcal{B}(\eta' \to \pi^+\pi^- e^+e^-)}$, at the 90% Confidence Level (C.L.) as a function of $M(a)$. The upper limits on the number of a signal events at the 90% C.L. are obtained according to the Bayesian method [51] by smearing the likelihood curve using a Gaussian function with a width of the systematic uncertainty as

$$L'(N) = \int_0^1 L\left(\frac{S}{\hat{S}}N\right) \exp\left[-\frac{(S-\hat{S})^2}{2\sigma_S^2}\right] dS, \tag{9.1}$$

where L and $L'(N)$ are the likelihood curves before and after taking into account the systematic uncertainties; $\hat{S}$ is the nominal efficiency and σ_S is its systematic uncertainty. As shown in figure 9, the limits on the branching ratio are established at the level of $(0.1 - 7.8) \times 10^{-3}$, and the significance for each case is less than 0.5σ.

10 Summary

With a sample of $(10087 \pm 44) \times 10^6$ J/ψ events, the branching fractions of $\eta' \to \pi^+\pi^- l^+ l^-$ (with $l = e, \mu$) are determined to be $\mathcal{B}(\eta' \to \pi^+\pi^- e^+e^-) = (2.45 \pm 0.02(\text{stat.}) \pm 0.08(\text{syst.})) \times 10^{-3}$ and $\mathcal{B}(\eta' \to \pi^+\pi^- \mu^+\mu^-) = (2.16 \pm 0.12(\text{stat.}) \pm 0.06(\text{syst.})) \times 10^{-5}$, which are in good agreement with the theoretical predictions [1, 4] and the previous measurements [5–8], as shown in figure 10 (a). The ratio of the branching fractions of these two decays is calculated to be $\frac{\mathcal{B}(\eta' \to \pi^+\pi^- e^+e^-)}{\mathcal{B}(\eta' \to \pi^+\pi^- \mu^+\mu^-)} = 113.4 \pm 0.9(\text{stat.}) \pm 3.7(\text{syst.})$.
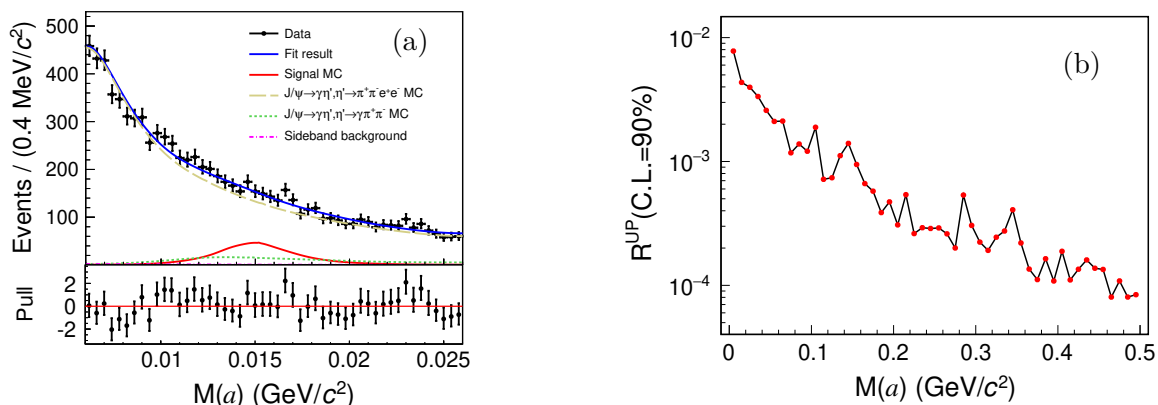
Figure 9. (a) Fit to the invariant mass distribution of M(a) when the mass of a is 15 MeV/c^2. The dots with error bars represent data, and the blue solid line is the total fit result. The red dashed histogram represents the arbitrary normalized MC signal shape, which is scaled by a factor of 10. The golden dashed histogram is the $J/\psi \to \gamma\eta', \eta' \to \pi^+\pi^- e^+ e^-$ MC shape. The green dashed histogram is the $J/\psi \to \gamma\eta', \eta' \to \gamma\pi^+\pi^-$ MC shape, and the pink dotted histogram is the background obtained from the η' sideband. (b) Upper limit on the relative branching ratio at the 90% C.L. for different a masses.

Additionally, we measure the TFF parameters of the η' decays, which are determined from the invariant decay amplitude of the reaction $\eta' \to \pi^+\pi^- l^+ l^-$. Our results are summarized in table 4. Since the previous experiment measured the parameters value of $c_1 - c_2$ and c_3 are approximately equal to 1 [48], we compared the results of Model I with other theoretical calculations and experimental measurements, which shown in figure 10 (b). In addition, we calculate a weighted average of $b_{\eta'} = 1.30 \pm 0.19$ (GeV/c^2)$^{-2}$ for $\eta' \to \pi^+\pi^- e^+ e^-$ and $\eta' \to \pi^+\pi^- \mu^+ \mu^-$ combined, where the uncertainty is obtained by combining statistical and systematic uncertainties. The value of $b_{\eta'}$ measured in this work is consistent with the VMD theoretical calculations [52] and the previous BESIII result [39], as shown in figure 10 (b). It indicates that the theoretical model used (Model I) is able to reasonably describe the process.

The CP-violating asymmetries of $\eta' \to \pi^+\pi^- l^+ l^-$ are determined to be $\mathcal{A}_{CP}(\eta' \to \pi^+\pi^- e^+ e^-) = (-0.21 \pm 0.73(\text{stat.}) \pm 0.01(\text{syst.}))\%$ and $\mathcal{A}_{CP}(\eta' \to \pi^+\pi^- \mu^+ \mu^-) = (0.62 \pm 4.71(\text{stat.}) \pm 0.08(\text{syst.}))\%$. These imply that no CP-violation evidence is found at the present level of statistics.

Finally, we perform a search for an ALP in the $e^+ e^-$ invariant mass spectrum, no significant signal is observed and the 90% C.L. upper limits of $\mathcal{B}^{\text{UP}}$ are shown in figure 9.
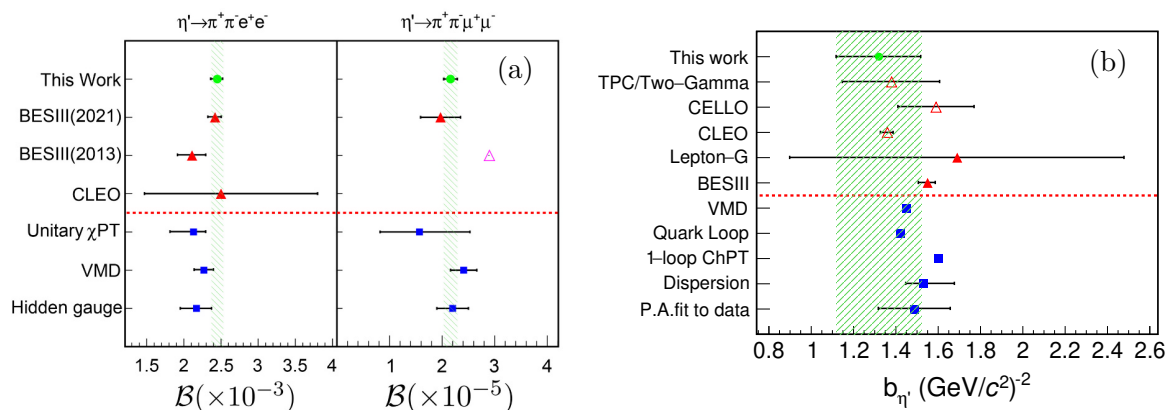
Acknowledgments

– 17 –

Figure 10. (a) The branching fractions of the $\eta' \to \pi^+\pi^-l^+l^-$ from different theoretical calculations [1, 4] (blue squares), the other experiments [5–8] (red solid and pink (90% C.L.) hollow triangles), and the results in our work (green dots). The upper limit of $\mathcal{B}(\eta' \to \pi^+\pi^-\mu^+\mu^-) < 2.4 \times 10^{-4}$ at the 90% C.L. is provided by the CLEO experiment [5]. (b) Slope parameter $b_{\eta'}$ for η' TFF from different theoretical calculations [3, 52–56](blue squares), time-like measurements [57–59](red solid triangles), space-like measurements [60–62] (red hollow triangles), and the results in our work (green dots).

References

[1] T. Petri, *Anomalous decays of pseudoscalar mesons*, Ph.D. thesis, University of Bonn, Bonn, Germany (2010) [arXiv:1010.2378] [INSPIRE].

[2] L. Gan, B. Kubis, E. Passemar and S. Tulin, *Precision tests of fundamental physics with η and η' mesons*, *Phys. Rept.* **945** (2022) 1 [arXiv:2007.00664] [INSPIRE].

[3] L. Ametller, J. Bijnens, A. Bramon and F. Cornet, *Transition form-factors in π^0, η and η and η' couplings to gamma gamma*, *Phys. Rev. D* **45** (1992) 986 [INSPIRE].

[4] B. Borasoy and R. Nissler, *η, $\eta' \to \pi^+\pi^- l^+ l^-$ in a chiral unitary approach*, *Eur. Phys. J. A* **33** (2007) 95 [arXiv:0705.0954] [INSPIRE].

[5] CLEO collaboration, *Observation of η' decays to $\pi^+\pi^-\pi^0$ and $\pi^+\pi^- e^+ e^-$*, *Phys. Rev. Lett.* **102** (2009) 061801 [arXiv:0809.2587] [INSPIRE].

[6] BESIII collaboration, *Measurement of $\eta' \to \pi^+\pi^- e^+ e^-$ and $\eta' \to \pi^+\pi^- \mu^+\mu^-$*, *Phys. Rev. D* **87** (2013) 092011 [arXiv:1303.7360] [INSPIRE].

[7] BESIII collaboration, *Observation of $\eta' \to \pi^+\pi^- \mu^+\mu^-$*, *Phys. Rev. D* **103** (2021) 072006 [arXiv:2012.04257] [INSPIRE].

[8] BESIII collaboration, *Measurement of the branching fraction of and search for a CP-violating asymmetry in $\eta' \to \pi^+\pi^- e^+ e^-$ at BESIII*, *Phys. Rev. D* **103** (2021) 092005 [arXiv:2011.07902] [INSPIRE].

[9] KTEV collaboration, *Observation of CP violation in $K_L \to \pi^+\pi^- e^+ e^-$ decays*, *Phys. Rev. Lett.* **84** (2000) 408 [hep-ex/9908020] [INSPIRE].

[10] G. Landini and E. Meggiolaro, *Study of the interactions of the axion with mesons and photons using a chiral effective Lagrangian model*, *Eur. Phys. J. C* **80** (2020) 302 [arXiv:1906.03104] [INSPIRE].

[11] D.S.M. Alves and S. Gonzàlez-Solís, *Final state rescattering effects in axio-hadronic η and η' decays*, arXiv:2402.02993 [INSPIRE].

[12] A.J. Krasznahorkay et al., *Observation of anomalous internal pair creation in ^8Be: a possible indication of a light, neutral boson*, *Phys. Rev. Lett.* **116** (2016) 042501 [arXiv:1504.01527] [INSPIRE].

[13] A.J. Krasznahorkay et al., *New evidence supporting the existence of the hypothetic X17 particle*, arXiv:1910.10459 [INSPIRE].

[14] D. Buttazzo, P. Panci, D. Teresi and R. Ziegler, *Xenon1T excess from electron recoils of non-relativistic dark matter*, *Phys. Lett. B* **817** (2021) 136310 [arXiv:2011.08919] [INSPIRE].

[15] U. Ellwanger and S. Moretti, *Possible explanation of the electron positron anomaly at $17\,MeV$ in ^8Be transitions through a light pseudoscalar*, *JHEP* **11** (2016) 039 [arXiv:1609.01669] [INSPIRE].

[16] J. Liu, N. McGinnis, C.E.M. Wagner and X.-P. Wang, *Challenges for a QCD axion at the $10\,MeV$ scale*, *JHEP* **05** (2021) 138 [arXiv:2102.10118] [INSPIRE].

[17] R.H. Parker et al., *Measurement of the fine-structure constant as a test of the Standard Model*, *Science* **360** (2018) 191 [arXiv:1812.04130] [INSPIRE].

[18] L. Morel, Z. Yao, P. Cladé and S. Guellati-Khélifa, *Determination of the fine-structure constant with an accuracy of 81 parts per trillion*, *Nature* **588** (2020) 61 [INSPIRE].

[19] NA64 collaboration, *Constraints on new physics in electron $g - 2$ from a search for invisible decays of a scalar, pseudoscalar, vector, and axial vector*, *Phys. Rev. Lett.* **126** (2021) 211802 [arXiv:2102.01885] [INSPIRE].

[20] BESIII collaboration, *Number of J/ψ events at BESIII*, *Chin. Phys. C* **46** (2022) 074001 [arXiv:2111.07571] [INSPIRE].

[21] BESIII collaboration, *Design and construction of the BESIII detector*, *Nucl. Instrum. Meth. A* **614** (2010) 345 [arXiv:0911.4960] [INSPIRE].

[22] C. Yu et al., *BEPCII performance and beam dynamics studies on luminosity*, in the proceedings of the 7th *international particle accelerator conference*, (2016) [DOI:10.18429/JACoW-IPAC2016-TUYA01] [InSPIRE].

[23] BESIII collaboration, *Future physics programme of BESIII*, *Chin. Phys. C* **44** (2020) 040001 [arXiv:1912.05983] [InSPIRE].

[24] P. Cao et al., *Design and construction of the new BESIII endcap time-of-flight system with MRPC technology*, *Nucl. Instrum. Meth. A* **953** (2020) 163053 [InSPIRE].

[25] GEANT4 collaboration, *GEANT4 — a simulation toolkit*, *Nucl. Instrum. Meth. A* **506** (2003) 250 [InSPIRE].

[26] J. Allison et al., *GEANT4 developments and applications*, *IEEE Trans. Nucl. Sci.* **53** (2006) 270 [InSPIRE].

[27] K.-X. Huang et al., *Method for detector description transformation to unity and application in BESIII*, *Nucl. Sci. Tech.* **33** (2022) 142 [arXiv:2206.10117] [InSPIRE].

[28] S. Jadach, B.F.L. Ward and Z. Was, *The precision Monte Carlo event generator K K for two fermion final states in e^+e^- collisions*, *Comput. Phys. Commun.* **130** (2000) 260 [hep-ph/9912214] [InSPIRE].

[29] S. Jadach, B.F.L. Ward and Z. Was, *Coherent exclusive exponentiation for precision Monte Carlo calculations*, *Phys. Rev. D* **63** (2001) 113009 [hep-ph/0006359] [InSPIRE].

[30] R.-G. Ping, *Event generators at BESIII*, *Chin. Phys. C* **32** (2008) 599 [InSPIRE].

[31] D.J. Lange, *The EvtGen particle decay simulation package*, *Nucl. Instrum. Meth. A* **462** (2001) 152 [InSPIRE].

[32] PARTICLE DATA GROUP collaboration, *Review of particle physics*, *PTEP* **2022** (2022) 083C01 [InSPIRE].

[33] J.C. Chen et al., *Event generator for J/ψ and $\psi(2S)$ decay*, *Phys. Rev. D* **62** (2000) 034003 [InSPIRE].

[34] R.-L. Yang, R.-G. Ping and H. Chen, *Tuning and validation of the Lundcharm model with J/ψ decays*, *Chin. Phys. Lett.* **31** (2014) 061301 [InSPIRE].

[35] Z.-Y. Zhang, L.-Q. Qin and S.-S. Fang, *Event generators for η/η' rare decays into $\pi^+\pi^-l^+l^-$ and $e^+e^-\mu^+\mu^-$*, *Chin. Phys. C* **36** (2012) 926 [InSPIRE].

[36] F.-K. Guo, B. Kubis and A. Wirzba, *Anomalous decays of η' and η into four pions*, *Phys. Rev. D* **85** (2012) 014014 [arXiv:1111.5949] [InSPIRE].

[37] BESIII collaboration, *Precision study of $\eta' \to \gamma\pi^+\pi^-$ decay dynamics*, *Phys. Rev. Lett.* **120** (2018) 242003 [arXiv:1712.01525] [InSPIRE].

[38] BESIII collaboration, *Measurement of the matrix elements for the decays $\eta' \to \eta\pi^+\pi^-$ and $\eta' \to \eta\pi^0\pi^0$*, *Phys. Rev. D* **97** (2018) 012003 [arXiv:1709.04627] [InSPIRE].

[39] BESIII collaboration, *Observation of the Dalitz decay $\eta' \to \gamma e^+e^-$*, *Phys. Rev. D* **92** (2015) 012001 [arXiv:1504.06016] [InSPIRE].

[40] Z.-R. Xu and K.-L. He, *A photon conversion finder at BESIII*, *Chin. Phys. C* **36** (2012) 742 [InSPIRE].

[41] PHENIX collaboration, *Detailed measurement of the e^+e^- pair continuum in p+p and Au+Au collisions at $\sqrt{s_{\mathrm{NN}}} = 200\,GeV$ and implications for direct photon production*, *Phys. Rev. C* **81** (2010) 034911 [arXiv:0912.0244] [InSPIRE].

[42] D.-N. Gao, *The CP violating asymmetry in* $\eta \to \pi^+\pi^- e^+ e^-$, *Mod. Phys. Lett. A* **17** (2002) 1583 [hep-ph/0202002] [INSPIRE].

[43] N. Cabibbo and A. Maksymowicz, *Angular correlations in* K_{e4} *decays and determination of low-energy* $\pi - \pi$ *phase shifts*, *Phys. Rev.* **137** (1965) B438 [*Erratum ibid.* **168** (1968) 1926] [INSPIRE].

[44] A. Pais and S.B. Treiman, *Pion phase-shift information from* $K_{\ell4}$ *decays*, *Phys. Rev.* **168** (1968) 1858 [INSPIRE].

[45] C. Picciotto and S. Richardson, *Chiral theory calculation of* $\eta \to \pi^+\pi^- e^+ e^-$, *Phys. Rev. D* **48** (1993) 3395 [INSPIRE].

[46] G.J. Gounaris and J.J. Sakurai, *Finite width corrections to the vector meson dominance prediction for* $\rho \to e^+ e^-$, *Phys. Rev. Lett.* **21** (1968) 244 [INSPIRE].

[47] C. Langenbruch, *Parameter uncertainties in weighted unbinned maximum likelihood fits*, *Eur. Phys. J. C* **82** (2022) 393 [arXiv:1911.01303] [INSPIRE].

[48] M. Benayoun, P. David, L. DelBuono and O. Leitner, *A global treatment of VMD physics up to the* ϕ: *I.* $e^+ e^-$ *annihilations, anomalies and vector meson partial widths*, *Eur. Phys. J. C* **65** (2010) 211 [arXiv:0907.4047] [INSPIRE].

[49] BESIII collaboration, *Search for hadronic transition* $\chi_{cJ} \to \eta_c \pi^+\pi^-$ *and observation of* $\chi_{cJ} \to K\overline{K}\pi\pi$, *Phys. Rev. D* **87** (2013) 012002 [arXiv:1208.4805] [INSPIRE].

[50] BESIII collaboration, *Observation of the Dalitz decay* $\eta' \to \gamma e^+ e^-$, *Phys. Rev. D* **92** (2015) 012001 [arXiv:1504.06016] [INSPIRE].

[51] Y.-S. Zhu, *Bayesian credible interval construction for Poisson statistics*, *Chin. Phys. C* **32** (2008) 363 [arXiv:0812.2705] [INSPIRE].

[52] A. Bramon and E. Masso, Q^2 *duality for electromagnetic form-factors of mesons*, *Phys. Lett. B* **104** (1981) 311 [INSPIRE].

[53] L. Ametller, L. Bergstrom, A. Bramon and E. Masso, *The quark triangle: application to pion and* η *decays*, *Nucl. Phys. B* **228** (1983) 301 [INSPIRE].

[54] C. Hanhart et al., *Dispersive analysis for* $\eta \to \gamma\gamma^*$, *Eur. Phys. J. C* **73** (2013) 2668 [*Erratum ibid.* **75** (2015) 242] [arXiv:1307.5654] [INSPIRE].

[55] R. Escribano, P. Masjuan and P. Sanchez-Puertas, η *and* η' *transition form factors from rational approximants*, *Phys. Rev. D* **89** (2014) 034014 [arXiv:1307.2061] [INSPIRE].

[56] S. Holz, C. Hanhart, M. Hoferichter and B. Kubis, *A dispersive analysis of* $\eta' \to \pi^+\pi^-\gamma$ *and* $\eta' \to \ell^+\ell^-\gamma$, *Eur. Phys. J. C* **82** (2022) 434 [*Addendum ibid.* **82** (2022) 1159] [arXiv:2202.05846] [INSPIRE].

[57] R.I. Dzhelyadin et al., *Observation of* $\eta' \to \mu^+\mu^-\gamma$ *decay*, *Phys. Lett. B* **88** (1979) 379 [INSPIRE].

[58] R.I. Dzhelyadin et al., *Investigation of* η *meson electromagnetic structure in* $\eta \to \mu^+\mu^-\gamma$ *decay*, *Phys. Lett. B* **94** (1980) 548 [INSPIRE].

[59] BESIII collaboration, *Improved measurements of the Dalitz decays* $\eta/\eta' \to \gamma e^+ e^-$, *Phys. Rev. D* **109** (2024) 072001 [arXiv:2401.09136] [INSPIRE].

[60] TPC/Two Gamma collaboration, *Investigation of the electromagnetic structure of* η *and* η' *mesons by two photon interactions*, *Phys. Rev. Lett.* **64** (1990) 172 [INSPIRE].

[61] CELLO collaboration, *A measurement of the* π^0, η *and* η' *electromagnetic form-factors*, *Z. Phys. C* **49** (1991) 401 [INSPIRE].

[62] CLEO collaboration, *Measurements of the meson-photon transition form-factors of light pseudoscalar mesons at large momentum transfer*, *Phys. Rev. D* **57** (1998) 33 [hep-ex/9707031] [INSPIRE].

The BESIII collaboration

M. Ablikim[1], M.N. Achasov[4,b], P. Adlarson[75], O. Afedulidis[3], X.C. Ai[80], R. Aliberti[35],
A. Amoroso[74A,74C], Q. An[71,58], Y. Bai[57], O. Bakina[36], I. Balossino[29A], Y. Ban[46,g], H.-R. Bao[63],
V. Batozskaya[1,44], K. Begzsuren[32], N. Berger[35], M. Berlowski[44], M. Bertani[28A], D. Bettoni[29A],
F. Bianchi[74A,74C], E. Bianco[74A,74C], A. Bortone[74A,74C], I. Boyko[36], R.A. Briere[5], A. Brueggemann[68],
H. Cai[76], X. Cai[1,58], A. Calcaterra[28A], G.F. Cao[1,63], N. Cao[1,63], S.A. Cetin[62A], J.F. Chang[1,58],
W.L. Chang[1,63], G.R. Che[43], G. Chelkov[36,a], C. Chen[43], C.H. Chen[9], Chao Chen[55], G. Chen[1],
H.S. Chen[1,63], M.L. Chen[1,58,63], S.J. Chen[42], S.L. Chen[45], S.M. Chen[61], T. Chen[1,63], X.R. Chen[31,63],
X.T. Chen[1,63], Y.B. Chen[1,58], Y.Q. Chen[34], Z.J. Chen[25,h], Z.Y. Chen[1,63], S.K. Choi[10], X. Chu[43],
G. Cibinetto[29A], F. Cossio[74C], J.J. Cui[50], H.L. Dai[1,58], J.P. Dai[78], A. Dbeyssi[18], R. E. de Boer[3],
D. Dedovich[36], C.Q. Deng[72], Z.Y. Deng[1], A. Denig[35], I. Denysenko[36], M. Destefanis[74A,74C],
F. De Mori[74A,74C], B. Ding[66,1], X.X. Ding[46,g], Y. Ding[34], Y. Ding[40], J. Dong[1,58], L.Y. Dong[1,63],
M.Y. Dong[1,58,63], X. Dong[76], M.C. Du[1], S.X. Du[80], Z.H. Duan[42], P. Egorov[36,a], Y.H. Fan[45],
J. Fang[59], J. Fang[1,58], S.S. Fang[1,63], W.X. Fang[1], Y. Fang[1], Y.Q. Fang[1,58], R. Farinelli[29A],
L. Fava[74B,74C], F. Feldbauer[3], G. Felici[28A], C.Q. Feng[71,58], J.H. Feng[59], Y.T. Feng[71,58], K. Fischer[69],
M. Fritsch[3], C.D. Fu[1], J.L. Fu[63], Y.W. Fu[1], H. Gao[63], Y.N. Gao[46,g], Yang Gao[71,58], S. Garbolino[74C],
I. Garzia[29A,29B], P.T. Ge[76], Z.W. Ge[42], C. Geng[59], E.M. Gersabeck[67], A. Gilman[69], K. Goetzen[13],
L. Gong[40], W.X. Gong[1,58], W. Gradl[35], S. Gramigna[29A,29B], M. Greco[74A,74C], M.H. Gu[1,58],
Y.T. Gu[15], C.Y. Guan[1,63], Z.L. Guan[22], A.Q. Guo[31,63], L.B. Guo[41], M.J. Guo[50], R.P. Guo[49],
Y.P. Guo[12,f], A. Guskov[36,a], J. Gutierrez[27], K.L. Han[63], T.T. Han[1], X.Q. Hao[19], F.A. Harris[65],
K.K. He[55], K.L. He[1,63], F.H. Heinsius[3], C.H. Heinz[35], Y.K. Heng[1,58,63], C. Herold[60], T. Holtmann[3],
P.C. Hong[12,f], G.Y. Hou[1,63], X.T. Hou[1,63], Y.R. Hou[63], Z.L. Hou[1], B.Y. Hu[59], H.M. Hu[1,63],
J.F. Hu[56,i], T. Hu[1,58,63], Y. Hu[1], G.S. Huang[71,58], K.X. Huang[59], L.Q. Huang[31,63], X.T. Huang[50],
Y.P. Huang[1], T. Hussain[73], F. Hölzken[3], N Hüsken[27,35], N. in der Wiesche[68], M. Irshad[71,58],
J. Jackson[27], S. Janchiv[32], J.H. Jeong[10], Q. Ji[1], Q.P. Ji[19], W. Ji[1,63], X.B. Ji[1,63], X.L. Ji[1,58],
Y.Y. Ji[50], X.Q. Jia[50], Z.K. Jia[71,58], D. Jiang[1,63], H.B. Jiang[76], P.C. Jiang[46,g], S.S. Jiang[39],
T.J. Jiang[16], X.S. Jiang[1,58,63], Y. Jiang[63], J.B. Jiao[50], J.K. Jiao[34], Z. Jiao[23], S. Jin[42], Y. Jin[66],
M.Q. Jing[1,63], X.M. Jing[63], T. Johansson[75], S. Kabana[33], N. Kalantar-Nayestanaki[64], X.L. Kang[9],
X.S. Kang[40], M. Kavatsyuk[64], B.C. Ke[80], V. Khachatryan[27], A. Khoukaz[68], R. Kiuchi[1],
O.B. Kolcu[62A], B. Kopf[3], M. Kuessner[3], X. Kui[1,63], A. Kupsc[44,75], W. Kühn[37], J.J. Lane[67],
P. Larin[18], L. Lavezzi[74A,74C], T.T. Lei[71,58], Z.H. Lei[71,58], H. Leithoff[35], M. Lellmann[35], T. Lenz[35],
C. Li[43], C. Li[47], C.H. Li[39], Cheng Li[71,58], D.M. Li[80], F. Li[1,58], G. Li[1], H. Li[71,58], H.B. Li[1,63],
H.J. Li[19], H.N. Li[56,i], Hui Li[43], J.R. Li[61], J.S. Li[59], Ke Li[1], L. J Li[1,63], L.K. Li[1], Lei Li[48], M.H. Li[43],
P.R. Li[38,k], Q.M. Li[1,63], Q.X. Li[50], R. Li[17,31], S.X. Li[12], T. Li[50], W.D. Li[1,63], W.G. Li[1], X. Li[1,63],
X.H. Li[71,58], X.L. Li[50], Xiaoyu Li[1,63], Y.G. Li[46,g], Z.J. Li[59], Z.X. Li[15], C. Liang[42], H. Liang[1,63],
H. Liang[71,58], Y.F. Liang[54], Y.T. Liang[31,63], G.R. Liao[14], L.Z. Liao[50], Y.P. Liao[1,63], J. Libby[26],
A. Limphirat[60], D.X. Lin[31,63], T. Lin[1], B.J. Liu[1], B.X. Liu[76], C. Liu[34], C.X. Liu[1], F.H. Liu[53],
Fang Liu[1], Feng Liu[6], G.M. Liu[56,i], H. Liu[38,j,k], H.B. Liu[15], H.M. Liu[1,63], Huanhuan Liu[1],
Huihui Liu[21], J.B. Liu[71,58], J.Y. Liu[1,63], K. Liu[38,j,k], K.Y. Liu[40], Ke Liu[22], L. Liu[71,58], L.C. Liu[43],
Lu Liu[43], M.H. Liu[12,f], P.L. Liu[1], Q. Liu[63], S.B. Liu[71,58], T. Liu[12,f], W.K. Liu[43], W.M. Liu[71,58],
X. Liu[38,j,k], X. Liu[39], Y. Liu[80], Y. Liu[38,j,k], Y.B. Liu[43], Z.A. Liu[1,58,63], Z.D. Liu[9], Z.Q. Liu[50],
X.C. Lou[1,58,63], F.X. Lu[59], H.J. Lu[23], J.G. Lu[1,58], X.L. Lu[1], Y. Lu[7], Y.P. Lu[1,58], Z.H. Lu[1,63],
C.L. Luo[41], M.X. Luo[79], T. Luo[12,f], X.L. Luo[1,58], X.R. Lyu[63], Y.F. Lyu[43], F.C. Ma[40], H. Ma[78],

H.L. Ma[1], J.L. Ma[1,63], L.L. Ma[50], M.M. Ma[1,63], Q.M. Ma[1], R.Q. Ma[1,63], X.T. Ma[1,63], X.Y. Ma[1,58], Y. Ma[46,g], Y.M. Ma[31], F.E. Maas[18], M. Maggiora[74A,74C], S. Malde[69], A. Mangoni[28B], Y.J. Mao[46,g], Z.P. Mao[1], S. Marcello[74A,74C], Z.X. Meng[66], J.G. Messchendorp[13,64], G. Mezzadri[29A], H. Miao[1,63], T.J. Min[42], R.E. Mitchell[27], X.H. Mo[1,58,63], B. Moses[27], N. Yu. Muchnoi[4,b], J. Muskalla[35], Y. Nefedov[36], F. Nerling[18,d], I.B. Nikolaev[4,b], Z. Ning[1,58], S. Nisar[11,l], Q.L. Niu[38,j,k], W.D. Niu[55], Y. Niu[50], S.L. Olsen[63], Q. Ouyang[1,58,63], S. Pacetti[28B,28C], X. Pan[55], Y. Pan[57], A. Pathak[34], P. Patteri[28A], Y.P. Pei[71,58], M. Pelizaeus[3], H.P. Peng[71,58], Y.Y. Peng[38,j,k], K. Peters[13,d], J.L. Ping[41], R.G. Ping[1,63], S. Plura[35], V. Prasad[33], F.Z. Qi[1], H. Qi[71,58], H.R. Qi[61], M. Qi[42], T.Y. Qi[12,f], S. Qian[1,58], W.B. Qian[63], C.F. Qiao[63], J.J. Qin[72], L.Q. Qin[14], X.S. Qin[50], Z.H. Qin[1,58], J.F. Qiu[1], S.Q. Qu[61], Z.H. Qu[72], C.F. Redmer[35], K.J. Ren[39], A. Rivetti[74C], M. Rolo[74C], G. Rong[1,63], Ch. Rosner[18], S.N. Ruan[43], N. Salone[44], A. Sarantsev[36,c], Y. Schelhaas[35], K. Schoenning[75], M. Scodeggio[29A], K.Y. Shan[12,f], W. Shan[24], X.Y. Shan[71,58], J.F. Shangguan[55], L.G. Shao[1,63], M. Shao[71,58], C.P. Shen[12,f], H.F. Shen[1,63], W.H. Shen[63], X.Y. Shen[1,63], B.A. Shi[63], H.C. Shi[71,58], J.L. Shi[12], J.Y. Shi[1], Q.Q. Shi[55], R.S. Shi[1,63], S.Y. Shi[72], X. Shi[1,58], J.J. Song[19], T.Z. Song[59], W.M. Song[34,1], Y. J. Song[12], S. Sosio[74A,74C], S. Spataro[74A,74C], F. Stieler[35], Y.J. Su[63], G.B. Sun[76], G.X. Sun[1], H. Sun[63], H.K. Sun[1], J.F. Sun[19], K. Sun[61], L. Sun[76], S.S. Sun[1,63], T. Sun[51,e], W.Y. Sun[34], Y. Sun[9], Y.J. Sun[71,58], Y.Z. Sun[1], Z.Q. Sun[1,63], Z.T. Sun[50], C.J. Tang[54], G.Y. Tang[1], J. Tang[59], Y.A. Tang[76], L.Y. Tao[72], Q.T. Tao[25,h], M. Tat[69], J.X. Teng[71,58], V. Thoren[75], W.H. Tian[59], Y. Tian[31,63], Z.F. Tian[76], I. Uman[62B], Y. Wan[55], S.J. Wang[50], B. Wang[1], B.L. Wang[63], Bo Wang[71,58], D.Y. Wang[46,g], F. Wang[72], H.J. Wang[38,j,k], J.P. Wang[50], K. Wang[1,58], L.L. Wang[1], M. Wang[50], Meng Wang[1,63], N.Y. Wang[63], S. Wang[12,f], S. Wang[38,j,k], T. Wang[12,f], T.J. Wang[43], W. Wang[72], W. Wang[59], W.P. Wang[71,58], X. Wang[46,g], X.F. Wang[38,j,k], X.J. Wang[39], X.L. Wang[12,f], X.N. Wang[1], Y. Wang[61], Y.D. Wang[45], Y.F. Wang[1,58,63], Y.L. Wang[19], Y.N. Wang[45], Y.Q. Wang[1], Yaqian Wang[17], Yi Wang[61], Z. Wang[1,58], Z.L. Wang[72], Z.Y. Wang[1,63], Ziyi Wang[63], D. Wei[70], D.H. Wei[14], F. Weidner[68], S.P. Wen[1], Y.R. Wen[39], U. Wiedner[3], G. Wilkinson[69], M. Wolke[75], L. Wollenberg[3], C. Wu[39], J.F. Wu[1,8], L.H. Wu[1], L.J. Wu[1,63], X. Wu[12,f], X.H. Wu[34], Y. Wu[71], Y.H. Wu[55], Y.J. Wu[31], Z. Wu[1,58], L. Xia[71,58], X.M. Xian[39], B.H. Xiang[1,63], T. Xiang[46,g], D. Xiao[38,j,k], G.Y. Xiao[42], S.Y. Xiao[1], Y. L. Xiao[12,f], Z.J. Xiao[41], C. Xie[42], X.H. Xie[46,g], Y. Xie[50], Y.G. Xie[1,58], Y.H. Xie[6], Z.P. Xie[71,58], T.Y. Xing[1,63], C.F. Xu[1,63], C.J. Xu[59], G.F. Xu[1], H.Y. Xu[66], Q.J. Xu[16], Q.N. Xu[30], W. Xu[1], W.L. Xu[66], X.P. Xu[55], Y.C. Xu[77], Z.P. Xu[42], Z.S. Xu[63], F. Yan[12,f], L. Yan[12,f], W.B. Yan[71,58], W.C. Yan[80], X.Q. Yan[1], H.J. Yang[51,e], H.L. Yang[34], H.X. Yang[1], Tao Yang[1], Y. Yang[12,f], Y.F. Yang[43], Y.X. Yang[1,63], Yifan Yang[1,63], Z.W. Yang[38,j,k], Z.P. Yao[50], M. Ye[1,58], M.H. Ye[8], J.H. Yin[1], Z.Y. You[59], B.X. Yu[1,58,63], C.X. Yu[43], G. Yu[1,63], J.S. Yu[25,h], T. Yu[72], X.D. Yu[46,g], C.Z. Yuan[1,63], J. Yuan[34], L. Yuan[2], S.C. Yuan[1], Y. Yuan[1,63], Z.Y. Yuan[59], C.X. Yue[39], A.A. Zafar[73], F.R. Zeng[50], S.H. Zeng[72], X. Zeng[12,f], Y. Zeng[25,h], Y.J. Zeng[59], Y.J. Zeng[1,63], X.Y. Zhai[34], Y.C. Zhai[50], Y.H. Zhan[59], A.Q. Zhang[1,63], B.L. Zhang[1,63], B.X. Zhang[1], D.H. Zhang[43], G.Y. Zhang[19], H. Zhang[71], H.C. Zhang[1,58,63], H.H. Zhang[59], H.H. Zhang[34], H.Q. Zhang[1,58,63], H.Y. Zhang[1,58], J. Zhang[59], J. Zhang[80], J.J. Zhang[52], J.L. Zhang[20], J.Q. Zhang[41], J.W. Zhang[1,58,63], J.X. Zhang[38,j,k], J.Y. Zhang[1], J.Z. Zhang[1,63], Jianyu Zhang[63], L.M. Zhang[61], Lei Zhang[42], P. Zhang[1,63], Q.Y. Zhang[39,80], Shuihan Zhang[1,63], Shulei Zhang[25,h], X.D. Zhang[45], X.M. Zhang[1], X.Y. Zhang[50], Y. Zhang[72], Y. T. Zhang[80], Y.H. Zhang[1,58], Y.M. Zhang[39], Yan Zhang[71,58], Yao Zhang[1], Z.D. Zhang[1], Z.H. Zhang[1], Z.L. Zhang[34], Z.Y. Zhang[76], Z.Y. Zhang[43], G. Zhao[1], J.Y. Zhao[1,63], J.Z. Zhao[1,58], Lei Zhao[71,58], Ling Zhao[1], M.G. Zhao[43], R.P. Zhao[63],

S.J. Zhao[80], Y.B. Zhao[1,58], Y.X. Zhao[31,63], Z.G. Zhao[71,58], A. Zhemchugov[36,a], B. Zheng[72], J.P. Zheng[1,58], W.J. Zheng[1,63], Y.H. Zheng[63], B. Zhong[41], X. Zhong[59], H. Zhou[50], J.Y. Zhou[34], L.P. Zhou[1,63], X. Zhou[76], X.K. Zhou[6], X.R. Zhou[71,58], X.Y. Zhou[39], Y.Z. Zhou[12,f], J. Zhu[43], K. Zhu[1], K.J. Zhu[1,58,63], L. Zhu[34], L.X. Zhu[63], S.H. Zhu[70], S.Q. Zhu[42], T.J. Zhu[12,f], W.J. Zhu[12,f], Y.C. Zhu[71,58], Z.A. Zhu[1,63], J.H. Zou[1], J. Zu[71,58]

[1] *Institute of High Energy Physics, Beijing 100049, People's Republic of China*

[2] *Beihang University, Beijing 100191, People's Republic of China*

[3] *Bochum Ruhr-University, D-44780 Bochum, Germany*

[4] *Budker Institute of Nuclear Physics SB RAS (BINP), Novosibirsk 630090, Russia*

[5] *Carnegie Mellon University, Pittsburgh, Pennsylvania 15213, U.S.A.*

[6] *Central China Normal University, Wuhan 430079, People's Republic of China*

[7] *Central South University, Changsha 410083, People's Republic of China*

[8] *China Center of Advanced Science and Technology, Beijing 100190, People's Republic of China*

[9] *China University of Geosciences, Wuhan 430074, People's Republic of China*

[10] *Chung-Ang University, Seoul, 06974, Republic of Korea*

[11] *COMSATS University Islamabad, Lahore Campus, Defence Road, Off Raiwind Road, 54000 Lahore, Pakistan*

[12] *Fudan University, Shanghai 200433, People's Republic of China*

[13] *GSI Helmholtzcentre for Heavy Ion Research GmbH, D-64291 Darmstadt, Germany*

[14] *Guangxi Normal University, Guilin 541004, People's Republic of China*

[15] *Guangxi University, Nanning 530004, People's Republic of China*

[16] *Hangzhou Normal University, Hangzhou 310036, People's Republic of China*

[17] *Hebei University, Baoding 071002, People's Republic of China*

[18] *Helmholtz Institute Mainz, Staudinger Weg 18, D-55099 Mainz, Germany*

[19] *Henan Normal University, Xinxiang 453007, People's Republic of China*

[20] *Henan University, Kaifeng 475004, People's Republic of China*

[21] *Henan University of Science and Technology, Luoyang 471003, People's Republic of China*

[22] *Henan University of Technology, Zhengzhou 450001, People's Republic of China*

[23] *Huangshan College, Huangshan 245000, People's Republic of China*

[24] *Hunan Normal University, Changsha 410081, People's Republic of China*

[25] *Hunan University, Changsha 410082, People's Republic of China*

[26] *Indian Institute of Technology Madras, Chennai 600036, India*

[27] *Indiana University, Bloomington, Indiana 47405, U.S.A.*

[28] *INFN Laboratori Nazionali di Frascati, (A)INFN Laboratori Nazionali di Frascati, I-00044, Frascati, Italy; (B)INFN Sezione di Perugia, I-06100, Perugia, Italy; (C)University of Perugia, I-06100, Perugia, Italy*

[29] *INFN Sezione di Ferrara, (A)INFN Sezione di Ferrara, I-44122, Ferrara, Italy; (B)University of Ferrara, I-44122, Ferrara, Italy*

[30] *Inner Mongolia University, Hohhot 010021, People's Republic of China*

[31] *Institute of Modern Physics, Lanzhou 730000, People's Republic of China*

[32] *Institute of Physics and Technology, Peace Avenue 54B, Ulaanbaatar 13330, Mongolia*

[33] *Instituto de Alta Investigación, Universidad de Tarapacá, Casilla 7D, Arica 1000000, Chile*

[34] *Jilin University, Changchun 130012, People's Republic of China*

[35] *Johannes Gutenberg University of Mainz, Johann-Joachim-Becher-Weg 45, D-55099 Mainz, Germany*

[36] *Joint Institute for Nuclear Research, 141980 Dubna, Moscow region, Russia*

[37] *Justus-Liebig-Universitaet Giessen, II. Physikalisches Institut, Heinrich-Buff-Ring 16, D-35392 Giessen, Germany*

[38] *Lanzhou University, Lanzhou 730000, People's Republic of China*

[39] *Liaoning Normal University, Dalian 116029, People's Republic of China*

[40] *Liaoning University, Shenyang 110036, People's Republic of China*

[41] *Nanjing Normal University, Nanjing 210023, People's Republic of China*

[42] *Nanjing University, Nanjing 210093, People's Republic of China*

[43] *Nankai University, Tianjin 300071, People's Republic of China*

^{44} National Centre for Nuclear Research, Warsaw 02-093, Poland

^{45} North China Electric Power University, Beijing 102206, People's Republic of China

^{46} Peking University, Beijing 100871, People's Republic of China

^{47} Qufu Normal University, Qufu 273165, People's Republic of China

^{48} Renmin University of China, Beijing 100872, People's Republic of China

^{49} Shandong Normal University, Jinan 250014, People's Republic of China

^{50} Shandong University, Jinan 250100, People's Republic of China

^{51} Shanghai Jiao Tong University, Shanghai 200240, People's Republic of China

^{52} Shanxi Normal University, Linfen 041004, People's Republic of China

^{53} Shanxi University, Taiyuan 030006, People's Republic of China

^{54} Sichuan University, Chengdu 610064, People's Republic of China

^{55} Soochow University, Suzhou 215006, People's Republic of China

^{56} South China Normal University, Guangzhou 510006, People's Republic of China

^{57} Southeast University, Nanjing 211100, People's Republic of China

^{58} State Key Laboratory of Particle Detection and Electronics, Beijing 100049, Hefei 230026, People's Republic of China

^{59} Sun Yat-Sen University, Guangzhou 510275, People's Republic of China

^{60} Suranaree University of Technology, University Avenue 111, Nakhon Ratchasima 30000, Thailand

^{61} Tsinghua University, Beijing 100084, People's Republic of China

^{62} Turkish Accelerator Center Particle Factory Group, (A)Istinye University, 34010, Istanbul, Turkey; (B)Near East University, Nicosia, North Cyprus, 99138, Mersin 10, Turkey

^{63} University of Chinese Academy of Sciences, Beijing 100049, People's Republic of China

^{64} University of Groningen, NL-9747 AA Groningen, The Netherlands

^{65} University of Hawaii, Honolulu, Hawaii 96822, U.S.A.

^{66} University of Jinan, Jinan 250022, People's Republic of China

^{67} University of Manchester, Oxford Road, Manchester, M13 9PL, United Kingdom

^{68} University of Muenster, Wilhelm-Klemm-Strasse 9, 48149 Muenster, Germany

^{69} University of Oxford, Keble Road, Oxford OX13RH, United Kingdom

^{70} University of Science and Technology Liaoning, Anshan 114051, People's Republic of China

^{71} University of Science and Technology of China, Hefei 230026, People's Republic of China

^{72} University of South China, Hengyang 421001, People's Republic of China

^{73} University of the Punjab, Lahore-54590, Pakistan

^{74} University of Turin and INFN, (A)University of Turin, I-10125, Turin, Italy; (B)University of Eastern Piedmont, I-15121, Alessandria, Italy; (C)INFN, I-10125, Turin, Italy

^{75} Uppsala University, Box 516, SE-75120 Uppsala, Sweden

^{76} Wuhan University, Wuhan 430072, People's Republic of China

^{77} Yantai University, Yantai 264005, People's Republic of China

^{78} Yunnan University, Kunming 650500, People's Republic of China

^{79} Zhejiang University, Hangzhou 310027, People's Republic of China

^{80} Zhengzhou University, Zhengzhou 450001, People's Republic of China

^{a} Also at the Moscow Institute of Physics and Technology, Moscow 141700, Russia

^{b} Also at the Novosibirsk State University, Novosibirsk, 630090, Russia

^{c} Also at the NRC "Kurchatov Institute", PNPI, 188300, Gatchina, Russia

^{d} Also at Goethe University Frankfurt, 60323 Frankfurt am Main, Germany

^{e} Also at Key Laboratory for Particle Physics, Astrophysics and Cosmology, Ministry of Education; Shanghai Key Laboratory for Particle Physics and Cosmology; Institute of Nuclear and Particle Physics, Shanghai 200240, People's Republic of China

^{f} Also at Key Laboratory of Nuclear Physics and Ion-beam Application (MOE) and Institute of Modern Physics, Fudan University, Shanghai 200443, People's Republic of China

^{g} Also at State Key Laboratory of Nuclear Physics and Technology, Peking University, Beijing 100871, People's Republic of China

^{h} Also at School of Physics and Electronics, Hunan University, Changsha 410082, China

^{i} Also at Guangdong Provincial Key Laboratory of Nuclear Science, Institute of Quantum Matter, South China Normal University, Guangzhou 510006, China

^{j} Also at MOE Frontiers Science Center for Rare Isotopes, Lanzhou University, Lanzhou 730000, People's Republic of China

^{k} Also at Lanzhou Center for Theoretical Physics, Lanzhou University, Lanzhou 730000, People's Republic of China

^{l} Also at the Department of Mathematical Sciences, IBA, Karachi 75270, Pakistan